DEFORMATION BEHAVIOR OF A535 ALUMINUM ALLOY

UNDER DIFFERENT STRAIN RATE AND TEMPERATURE CONDITIONS

A Thesis Submitted to the College of

Graduate Studies and Research

in Partial Fulfillment of the Requirements

for the Degree of Master of Science

in the Department of Mechanical Engineering

University of Saskatchewan

Saskatoon

By

Mojgan Rezaei

.

PERMISSION TO USE

In presenting this thesis/dissertation in partial fulfillment of the requirements for a Postgraduate degree from the University of Saskatchewan, I agree that the libraries of this University may make it freely available for inspection. I further agree that permission for copying of this thesis/dissertation in any manner, in whole or in part, for scholarly purposes may be granted by the professor or professors who supervised my thesis/dissertation work or in their absence, by the Head of the Department or the Dean of the College in which my thesis work was done. It is understood that any copying or publication or use of this thesis/dissertation or parts thereof for financial gain shall not be allowed without my written permission. It is also understood that due recognition shall be given to me and to the University of Saskatchewan in any scholarly use which may be made of any material in my thesis/dissertation.

Request for permission to copy or to make other uses of materials in this thesis/dissertation in whole or part should be addressed to:

Head of the Department of Mechanical Engineering

57 Campus Drive

University of Saskatchewan

Saskatoon, Saskatchewan S7N 5A9

Canada

ABSTRACT

Aluminum alloys are a suitable substitution for heavy ferrous alloys in automobile structures. The purpose of this study was to investigate the flow stress behavior of as-cast and homogenized A535 aluminum alloy under various deformation conditions. A hot compression test of A535 alloy was performed in the temperature range of 473-673 K (200-400˚C) and strain rate range of 0.005-5 s^{-1} using a Gleeble^{TM} machine. Experimental data were fitted to Arrhenius-type constitutive equations to find material constants such as n, n', β, A and activation energy (Q). Flow stress curves for as-cast and homogenized A535 alloy were predicted using an extended form of the Arrhenius constitutive equations. The dynamic shock load response of the alloy was studied using a split Hopkinson pressure bar (SHPB) test apparatus. The strain rate used ranged from 1400 s^{-1} to 2400 s^{-1} for as-cast and homogenized A535 alloy. The microstructures of the deformed specimens under different deformation conditions were analyzed using optical microscopy (OM) and scanning electron microscopy (SEM).

Obtained true stress-true strain curves at elevated temperatures showed that the flow stress of the alloy increased by increasing the strain rate and decreasing the temperature for both as-cast and homogenized specimens. The homogenization heat treatment showed no effect on the mechanical behavior of the A535 alloy under hot deformation conditions. Hot deformation activation energy for both as-cast and homogenized A535 alloy was calculated to be 193 kJ/mol, which is higher than that for self-diffusion of pure aluminum (142 kJ/mol). The calculated stress values were compared with the measured ones and they showed good agreement by the correlation coefficient (R) of 0.997 and the average absolute relative error (AARE) of 6.5 %.

The peak stress and the critical strain at the onset of thermal softening increased with strain rate for both the as-cast and homogenized A535 alloy. Homogenization heat treatment affected the high strain-rate deformation of the alloy, by increasing the peak stress and the thermal softening onset strain compared to those obtained for as-cast specimens. Deformed shear bands (DSBs) were formed in both the as-cast and homogenized A535 alloy in the strain rate range of 2000-2400 s^{-1}.

PERMISSION TO REPRODUCE

Permission to use Figure 2.2:

The received copyright permission information:

License Number	3443431350844
License date	August 07, 2014
Licensed content publisher	Elsevier
Licensed content publication	Materials Science and Engineering: A
Licensed content title	Evolution of activation energy during hot deformation of AA7150 aluminum alloy
Licensed content author	Cangji Shi, Weimin Mao and X.Grant Chen
Licensed content date	June 01, 2013
Licensed content volume number	571
Licensed content issue number	n/a
Number of pages	9
Type of Use	reuse in a thesis/dissertation
Portion	figures/tables/illustrations
Number of figures/tables/illustrations	1
Format	both print and electronic
Are you the author of this Elsevier article?	No
Will you be translating?	No
Title of your thesis/dissertation	Deformation behavior of aluminum alloy A535 under different strain rate and temperature conditions
Expected completion date	August, 2014
Estimated size (number of pages)	100
Elsevier VAT number	GB 494 6272 12
Permissions price	0.00 USD
VAT/Local Sales Tax	0.00 USD / 0.00 GBP
Total	0.00 USD

Permission to use Figures 2.3 and 2.4:

Summary:

Title	Measurement of the deformation of aluminum alloys under high strain rates using high speed digital cameras
Author	Gbadebo Owolabi, Daniel Odoh, Alex Peterson, Akindele Odeshi and Horace Whitworth
Source (DOI number)	10.4236/wjm.2013.32009
License	Copyright © 2013 Gbadebo Owolabi et al. This is an open access article distributed under the Creative Commons Attribution License, which permits unrestricted use, distribution, and reproduction in any medium, provided the original work is properly cited.

From:	**Owolabi, Gbadebo** <gbadebo.owolabi@howard.edu>
To:	mojgan rezaei <mor473@mail.usask.ca>
Date:	Sat, Aug 30, 2014 at 3:50 PM
Subject:	RE: Copyright Permission

Hello

Yes, you have my permission to use the Figure 18 of the paper. Please do not forget to reference the paper.

All the best.
Dr. Owolabi

ACKNOWLEDGEMENTS

I would like to acknowledge many people for their supports during my research. First, I would like to thank my supervisor Professor Ike Oguocha for his useful comments, remarks and engagement which greatly improved my work. Secondly, I would also like to thank the Head of the Mechanical Engineering Department Dr. Jim Bugg. I would like to express my gratitude to my advisory committee members, Professors Akindele Odeshi and Reza Fotouhi for their technical support and important suggestions and many thanks to Mr. Hamed Asgari for his invaluable guidance and time spent in helping me to complete my second part of the experiments and Mr. Robert Peace for his assistance during experimental difficulties.

Many thanks go to Professor Olanrewaju Ojo and members of his research group, Dr. Soheyl Soleymani and Mr. Michael Boswick, for providing the opportunity to use Gleeble machine in the Department of Mechanical Engineering at the University of Manitoba.

Finally, my endless gratitude goes to my beloved husband for his love, support, encouragement and understanding, my parents and my friends for giving me extra strength and motivation by keeping me harmonious and helping me putting pieces together.

DEDICATION

This thesis is dedicated to my parents for their love and support throughout my life. Thank you both for giving me strength to reach for the stars and chase my dreams.

TABLE OF CONTENTS

LIST OF TABLES

LIST OF FIGURES

LIST OF SYMBOLS

Symbols	Unit	Description
σ_e	MPa	Engineering stress
σ_T	MPa	True stress
σ_P	MPa	Peak stress
σ_S	MPa	Saturated stress
σ_{SS}	MPa	Steady-state stress
σ_M	MPa	Measured stress
σ_C	MPa	Calculated stress
e	mm/mm	Engineering strain
$\dot{\varepsilon}$	s^{-1}	Engineering strain rate
ε_T	mm/mm	True strain
ε_R	mm/mm	Reflected strain
ε_T	mm/mm	Transmitted strain
α	MPa^{-1}	Stress multiplier
β	MPa^{-1}	Material constant
A	s^{-1}	Material constant
A'	$s^{-1}\,MPa^{-1}$	Material constant
A''	s^{-1}	Material constant
A_B	mm^2	Cross sectional area of the bar
A_S	mm^2	Cross sectional area of the specimen
C_B	m/s	Velocity of sound in the bar
D	Mm	Diameter of the specimen
E_B	GPa	Elastic modulus of the bar
h		Hour
L	Mm	Length of the specimen
m	---	Strain rate sensitivity
n	---	Material constant
n'	---	Material constant

Q	J/mol	Activation energy
R	J /mol.K	Universal gas constant
R		Correlation coefficient
R^2		Square of residuals
S	K	Material constant
T	K	Absolute temperature
T_m	K	Absolute melting temperature
T2		Temper designation
T4		Temper designation
T6		Temper designation
T8		Temper designation
t	S	Time
Z	s^{-1}	Zener-Hollomon parameter

LIST OF ABBREVIATIONS

AARE	Absolute average relative error
ASB	Adiabatic shear band
ASTM	American society for testing and materials
CAFE	Corporate average fuel economy
CGS	Centimeter-gram-second
DPN	Dynamic precipitation
DRV	Dynamic recovery
DRX	Dynamic recrystallization
DSB	Deformed shear band
EPA	Environmental protection agency
ECA	Equal channel angular
FCC	Face centered cubic
GHG	Greenhouse gas
HAB	High angle boundary
IACS	International annealed copper standard
ICP-MS	Inductively coupled plasma-mass spectrometry
OM	optical microscopy
NHTSA	National highway traffic safety administration
SEM	Scanning electron microscope
SHPB	Split Hopkinson pressure bar
SHS	Sintering and synthesis
SICO	Strain induced crack opening
TEM	Transmission electron microscopy
TSB	Transformed shear band
wt.%	Weight percent

CHAPTER 1

INTRODUCTION

1.1 Overview

The demand for fuel efficient automobiles in order to reduce fuel consumption and environmental degradation is growing nowadays. The US [1], Japan and European countries [2] have introduced strict rules for automobile manufacturers to reduce greenhouse gas (GHG) emissions. For instance, the European commission declared that the rate of CO_2 emission has to be decreased to 140 g/km or less by 2008 and to 130 g/km by 2012. The U.S. Environmental Protection Agency (EPA) and the Department of Transportation's National Highway Traffic Safety Administration (NHTSA) have taken serious measures to decrease GHG emissions and fuel consumption of light duty vehicles [3]. EPA has introduced national GHG emissions standards according to the Clean Air Act in 1970. The US congress established Corporate Average Fuel Economy (CAFE) standards in 1975 and authorized NHTSA to declare these standards according to the Energy Policy and Conservation Act [4]. NHTSA has established the new standard to extend the fuel reduction policy. Since 60 percent of fuel consumption and GHG emissions are associated with light duty vehicles in the US, the EPA's standards mandated automobile manufacturers to reach a level of 102 g/km of carbon dioxide (CO_2) emission by 2025. Under the new standards, it is estimated that vehicles' emissions level drops approximately by 2 billion metric tons with a benefit to society up to $326-451 billions [5]. By meeting the requirements of these standards, families will benefit $1.7 [5] trillion from reduction in fuel cost, and the US will save 2 billion barrels per day by 2025.

Automakers have made huge progress in finding a feasible solution to reduce the fuel consumption of automobiles. Weight reduction was found as a suitable way because a lighter vehicle needs less energy to accelerate. Although ferrous alloys (steel and cast-iron) have extensively been used in automobile structures for a long time, they suffer from high density which leads to high weight of parts made from them. Materials with lower density than steel such as aluminum alloys, magnesium alloys, carbon fiber reinforced polymers and injection molded plastics are considered suitable alternatives for reducing automobile weight [1]. Among these materials, aluminum alloys are recognized as a very attractive replacement for ferrous

alloys due to their high strength-to-weight ratio, excellent corrosion resistance, good formability, and recyclability [6]. Reducing 100 kg of the car weight can lower GHG emissions by 9 grams per kilometer [7]. Replacing heavy parts of automobile parts with aluminum alloys can possibly decrease its weight by 50 percent [7].

A large amount of aluminum (about 81 percent) is currently used in casting form for manufacturing engine blocks, cylinder heads, wheels, heat exchangers, casings for transmission system, and control arms in the chassis. Lately, they are being considered for producing space frames, axle parts and structural components of automobiles [8]. The aluminum share in the automobile industry was projected to increase from 142 kg in 2007 to 170 kg per vehicle in 2020 [9].

1.2 Motivation

A535 is a cast aluminum-magnesium alloy which demonstrates potential applicability in fabricating automobile body parts and engine components such as engine block, pistons, cylinders, cylinders heads, cylinder liners and brake calipers. It possesses a better combination of strength, shock resistance and ductility than any other non-heat treatable cast aluminum alloy and the original properties remain the same even after stress relieving operation [10]. However, there is little knowledge of its deformation behavior under elevated temperature and high strain rate loading conditions, which would be useful for high temperature resistant and crash absorbent applications in automobiles.

1.3 Objectives

The main objectives of this research were:

1. To determine the deformation behavior of A535 alloy at elevated temperatures and low strain rates.
2. To determine the flow stress behavior of as-cast and homogenized A535 alloy under high strain rate deformation condition at room temperature.
3. To determine the effect of heat treatment on the deformation behavior of A535 alloy under hot deformation and high strain rate deformation conditions.
4. To determine changes in microstructures developed in specimens tested under hot deformation and high strain rate deformation conditions.

1.4 Thesis Outline

The first chapter explains the thesis background, motivation and objectives. The second chapter presents the pertinent literature review. The third chapter describes the test material and experimental procedures. The fourth chapter presents and discusses the obtained experimental and numerical results. The fifth chapter presents the conclusions and recommendations for future research.

CHAPTER 2

LITERATURE REVIEW

This chapter presents a review of the pertinent literature related to the topics pursued in the present research. It covers basic review of aluminum alloys and detailed review of hot deformation of metals at elevated temperatures and low strain rates as well as high strain rate deformation at room temperature.

2.1 Aluminum Alloys

Pure aluminum has a silvery-white surface, high light and heat reflectivity. The density of aluminum at room temperature is 2.7 g/cm^3, but it decreases to 2.6 g/cm^3 at the temperature of 660˚C, near the melting point, and 2.4 g/cm^3 for the molten metal [10]. Its thermal conductivity is 209 W/m.K, but a small amount of impurities has adverse effect on its conductivity. The prominent properties of aluminum alloys which make them attractive for a wide range of applications are light weight, good formability, adequate mechanical properties and excellent corrosion resistance [10]. Aluminum alloys are classified in two main groups based on the way they are processed or produced, namely: cast and wrought alloys. Wrought aluminum alloys are used for various forming processes such as rolling, extrusion and forging. The cast grades are used for castings. Cast alloys are fabricated in different ways including sand casting, mold casting, and die casting. The main difference between wrought and cast aluminum alloys is the structure and texture, which are essentially isotropic for cast alloys [10].The chemical composition of cast alloys are different from wrought alloys of the same grade due to the different method of manufacturing. The cast aluminum alloys are utilized in engine parts, kitchen

appliances and aircraft body structures. Wrought alloys are fabricated in the form of worked products such as sheets, plates, foils, tubes, rods, bar and wires [10].

Both wrought and cast aluminum alloys are divided into two groups: heat treatable and non-heat treatable. The strength and hardness of heat treatable alloys can be improved through a three-stage heat treatment, namely: solution heat treatment, quenching and age hardening. Non-heat treatable alloys gain strength by either strain hardening or solid solution strengthening [11].

2.1.1 Aluminum-Magnesium Alloys

Magnesium is a common alloying element in aluminum alloys due to its excellent solubility, which can be up to 7 wt. % in wrought, and up to 10 wt.% in cast aluminum alloys. As the solubility of magnesium decreases by lowering temperature, the excess solute precipitates out of the matrix in the form of the β-phase (Mg_2Al_3) along the grain boundaries which raises the stress corrosion cracking susceptibility [12].

The compressive strength of Al-Mg alloys is roughly equal to the tensile strength. The shear strength is in the range of 70-80% of tensile strength [11]. The notch toughness of cast alloys is low especially in alloys with high Mg content, but wrought aluminum alloys with low magnesium content show good toughness. In cast alloys, due to the existence of brittle phases at grain boundaries, ductility and toughness are low and are decreased at temperatures below 0˚C [13].

2.1.2 A535 Aluminum Alloy

A535 is a cast Al-Mg alloy which displays a superior combination of strength, shock resistance and ductility compared to any other as cast non-heat treatable aluminum alloys. It is customary to use it directly after casting, without any further heat treatment or natural aging. The original properties remain virtually the same even after a stress relieving operation (T2 condition) [10]. The liquidus and solidus temperatures are respectively 630˚C and 550˚C. Typical physical and mechanical properties of the A535 aluminum alloy are shown in Table 2.1. The mechanical properties of this alloy can be improved by solution heat treatment at 400˚C for 5 hours [14]. Usually, some internal stress is present as a result of high cooling rate from the liquid temperature during solidification or after heat treatment which may lead to distortion of the component after machining. It is usually fabricated by sand or permanent mold casting.

Table 2.1. Typical physical and mechanical properties of A535 aluminum alloy [14].

Density	2.62 g/cm3
Electrical conductivity	23 % IACS[*1]
Thermal conductivity at 25˚C	0.23 CGS[*2]
Tensile strength	240 MPa
Yield strength	125 MPa
Elongation percent in 51 mm	8.0%
Brinell hardness	60-70
Charpy impact energy	14.2 J
Compressive yield strength	162 MPa

*1. IACS stands for the International Annealed Copper Standard.
*2. CGS stands for Centimeter-Gram-Second.

A535 aluminum alloy has a good dimensional stability which makes it perfect for high speed machining. High microfinishes are attainable at high speeds and it yields mirror polish. A535 can be welded using any inert gas shielded-arc systems. The reasonably good impact energy of A535 alloy makes it appropriate for high vibrational shock load applications such as aircraft landing gears, rocket launchers and lightweight armored vehicles. Its high dimensional stability makes it suitable for use in computing devices and electronic equipment. A535 is relatively more expensive and sophisticated to fabricate than the majority of cast aluminum alloys, but this is compensated by omitting heat treatment and simpler finishing operations [10].

2.2 Recovery and Recrystallization

When a metal is plastically deformed, a certain amount of energy is stored internally by dislocations generated in the material. This energy can be released through different ways such as recovery, recrystallization and coarsening. Recovery refers to the lowering of the stored energy by dislocation annihilation and rearrangement to a position with lower level of energy without any change in high angle grain boundaries (HAB). Recrystallization is the formation of new strain-free grains by evolution and movement of high angle grain boundaries. Coarsening is the growth of original grains by which the strength of material is decreased by lowering the total grain boundary surface area.

The softening mechanisms usually activate at temperatures approximately 0.5 T_m (where T_m = the absolute melting temperature of the material). Hence, during hot deformation process both work hardening and softening compete to control the flow stress. The recovery and recrystallization mechanisms which occur during deformation are called dynamic recovery (DRV) and dynamic recrystallization (DRX), respectively. Rising flow stress is a sign of work hardening domination, while a flat stress level indicates that work hardening and flow softening are at an equilibrium state. A declining flow stress shows that flow softening has surpassed work hardening [15].

2.3 Deformation Behavior of Metals at Elevated Temperatures and Low Strain Rates

The quasi-static deformation behavior of various metallic materials has frequently been investigated by following three main steps. The first is conducting compression tests under defined temperatures and strain rates to produce stress-strain curves. Analyzing the obtained curves helps to understand the mechanical properties of the tested material under the test

conditions. The apparatus which is often used is either Instron machine or Gleeble machine. In the second step, the obtained experimental data can be fitted to different constitutive equations which are widely applicable to hot deformation processes to derive some material constants. The third is microstructural examination of deformed specimen which helps to understand the influence of deformation temperature and strain rate on the microstructure.

2.3.1 Stress-Strain Curves

One of the common methods for investigating hot deformation behavior of a material is to conduct either tensile or compression test under prescribed thermo-mechanical condition. Recording load-displacement data of the specimen during the deformation by computerized data acquisition system helps to generate the stress-strain curve of the material, which is a very important feature of this test. Although the trend of the experimentally determined stress-strain curves might be different for various alloys, two deformation mechanisms usually control the flow behavior of materials namely, work hardening and strain softening. As the material used for this research is an aluminum alloy, the majority of the presented literature was selected from hot deformation behavior of aluminum alloys.

It is frequently reported that stress-strain curves of aluminum alloys which had undergone hot deformation follow two trends. Figure 2.1 shows a hypothetical stress strain diagram of an aluminum alloy under hot deformation condition. The flow stress initially increases due to work hardening, then it reaches a peak (σ_p), after which it attains a constant stress (case a) called saturated stress (σ_s), or it exhibits firstly a decline (case b) followed by a steady-state stress shown as (σ_{ss}) [16]. Quan et al. [17] performed a set of hot compression tests on as-extruded

7075 aluminum alloy in temperature ranges of 573 to 673 K and strain rate range of 0.01 to 10 s^{-1} to determine the mechanical response of the alloy under different deformation conditions. The obtained stress-strain curves showed that the flow stress of the alloy was sensitive to both strain rate and temperature. Furthermore, under all the test conditions, the flow stress increased rapidly initially and after reaching a peak it showed a gradual decline to the end of deformation. Microstructural observations indicated dynamic recrystallization (DRX) occurrence after passing the peak stress.

Jin et al. [18] reported that the dominant deformation mechanism for AA7150 aluminum alloy at high *Z* value (high strain rate and low temperature) was dynamic precipitation (DPN), while at low *Z* values (low strain rate and high temperature) was a combination of DRV and DRX. However, Shi et al. [19] reported that DRV mostly controlled the deformation of AA7150 aluminum alloy under hot deformation conditions. A similar behavior was found for AA7050 aluminum alloy [20].

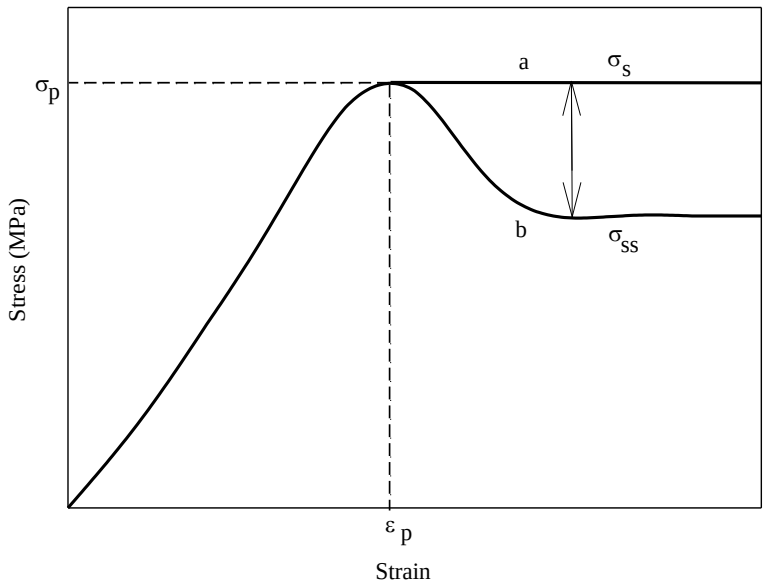

Figure 2.1. Schematic of stress-strain curves of aluminum alloys under hot compression deformation conditions (adapted from Reference [16]).

Figure 2.2 shows stress-strain curves obtained for AA7150 aluminum alloy under different deformation conditions [19]. Li et al. [21] observed that the flow stress behavior of 7050 aluminum alloy increased with increasing strain rate and decreasing temperature. The stress level remained flat or rose after the initial peak at strain rates lower or higher than 1 s^{-1}, respectively. Therefore, DRV was the main softening mechanism at low strain rates, while DRX and DRV controlled deformation at high strain rates. Similar stress-strain curve trends were reported for aluminum alloys A357 [22], A356 [23], AA5052 [24], and AA5182 [25] under elevated temperature and low strain rate conditions, while DRV

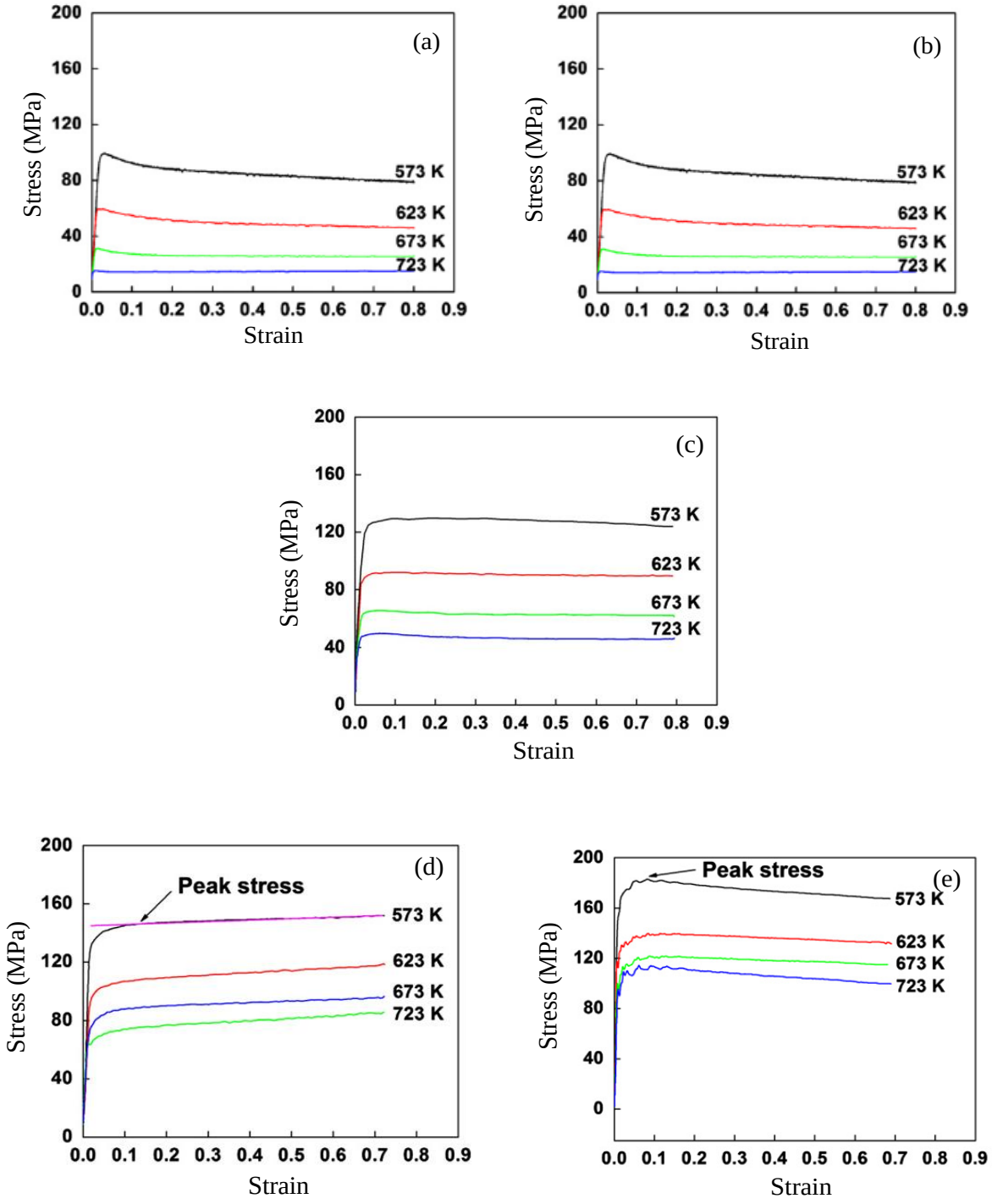

Figure 2.2. True stress-true strain curves of AA7150 aluminum alloy at strain rates of (a) 0.001 s^{-1} (b) 0.01 s^{-1} (c) 0.1 s^{-1} (d) 1 s^{-1} (e) 10 s^{-1} [19].

was found to be the main softening mechanisms at lower strain rate and higher temperature, DRX was responsible for flow softening at higher strain rate and temperature. Ebrahimi et al. [26] studied the deformation behavior of AA2024 aluminum alloy under quasi-static loading after solution heat treatment and annealing. It was shown that the effect of thermal treatment at high temperatures and low strain rates was minimal. However, at a temperature of 350˚C strain softening of the solution heat treated specimen was much higher than the annealed specimens, because of removal of solute atoms of the matrix and coarsening precipitates. Similar results were reported for homogenized and solution treated AA7085 [27], AA6082 [28], AA6201 [29] and AA2219 [30] aluminum alloys under elevated temperature quasi-static test loading. Gang et al. [31] suggested that the addition of erbium (Er) element to Al-5.7Mg substantially changed the mechanical behavior of the alloy at high temperatures. Analysis of the flow stress curves and microstructures showed that dynamic recrystallization (DRX) occurrence was restricted by Al_3Er particles, which formed within the matrix. These particles impeded dislocation movement and grain boundary sliding at high temperatures. Hence, the addition of Er to Al-5.7Mg alloy makes it possible for this alloy to be used for high temperature resistant structures. Li et al. [32] found that the mechanical behavior of Ag-containing AA2519 aluminum alloy was affected by deformation temperature and strain rate. Microstructural observations indicated that the deformation mechanism switched from DRV at low strain rates and temperatures to DRX at higher strain rate and temperature. The driving force for DRX occurrence was supplied by the energy of piled up dislocations which were unable to rearrange themselves within a short time at high strain rate deformation. Similar results were reported for Al-Mg-Si-Cu, Al-Zn-Mg-Cu aluminum alloys under hot deformation circumstances [33, 34].

2.3.2 Constitutive Equations

In order to simulate the plastic deformation behavior of a metal at different temperatures and low strain rates, different types of models and constitutive equations have been proposed. These mathematical models measure the effectiveness of parameters such as strain, strain rate, temperature, work hardening and flow softening on flow stress during hot deformation [35].

All constitutive equations can be divided into the following two main groups:

1. Phenomenological constitutive models (i.e. flow stress versus plastic strain data). The flow stress is described in terms of experimental data and some mathematical formulas are involved as well. Physical mechanisms associated with the deformation such as thermally activated dislocation motion are ignored to reduce the complexity of mathematical formulization as well as the number of material parameters to be calculated [36].

2. Physical constitutive models. In contrast to phenomenological model, a physical model considers mechanisms associated with the dynamic deformation of the material such as thermodynamics and kinetics of dislocation movements. Since many mechanisms are considered, these models require complicated formulization and a large number of material parameters to be determined experimentally [37].

One of the widely applied phenomenological constitutive models for hot deformation of metals is the Arrhenius-type equation (2.1) [38], through which strain rate and deformation temperature are related to the flow stress.

$$\dot{\varepsilon} = AF(\sigma)\exp\left(\frac{-Q}{RT}\right) \tag{2.1}$$

The effects of strain rate and temperature on flow stress can be simultaneously represented by the Zener-Hollomon parameter (*Z* value) as shown in equation (2.2) [39], where, $\dot{\varepsilon}$ is the strain rate (s^{-1}), *Z* is the Zener-Hollomon parameter (s^{-1}), *Q* is the activation energy for hot deformation of material (J/mol), *R* is the universal gas constant (8.31 J/mol.K), σ is the flow stress (MPa), *T* is the absolute temperature (K), and *A* is a material constant (s^{-1}). As shown in equation (2.1), strain rate is expressed as a function of the flow stress. The flow stress can be rewritten in three ways, as shown in equation (2.3).

$$Z = \dot{\varepsilon} \exp\left(\frac{Q}{RT}\right) \tag{2.2}$$

$$F(\sigma) = \begin{cases} \sigma^{n'} & \alpha\sigma < 0.8 \\ \exp(\beta\sigma) & \alpha\sigma > 1.2 \\ [\sinh(\alpha\sigma)]^{n} & all\ \sigma \end{cases} \tag{2.3}$$

where α (MPa^{-1}) is stress multiplier (α = β/*n*), *n*, *n′* and β (MPa^{-1}) are material constants. The power law relation of equation (2.3) is a suitable relation for low stress; the exponential type is used for high level of stress; and the hyperbolic sine type is used for a wide range of stress [40].

A close examination of the constitutive equations shows that the effect of strain rate and deformation temperature is merely considered in predicting material constants. Shi et al. [19] calculated the material constants of AA7150 alloy utilizing Arrhenius-type equations in which experimental data were fitted to this equation. It was found that material constants such as activation energy were influenced by the deformation temperature. The activation energy of this alloy varied from 500 kJ/mol to 81 kJ/mol at the lowest and highest temperatures, respectively. It

was demonstrated that strain has a prominent influence on the deformation behavior of the Al-Zn-Mg-Cu aluminum alloy. The activation energy of Al-Zn-Mg-Cu varied in the range of 136.61 to 143.31 kJ/mol [34], which is close to the self-diffusion of pure aluminum alloy [41].

The Zener-Hollomon parameter is widely applied to determine the effect of deformation temperature and strain rate on the peak stress of variety of alloys under hot deformation conditions. In addition, by substituting obtained material constants and Z values in the constitutive equations, peak stress values can be predicted theoretically. This procedure has been successful in correlating measured and predicted values in homogenized AA7050 [20], AA7150 [18], AA7075 [42], Al-Cu-Mg [43], and AA3003 aluminum alloys [44].

Lin et al. [45] also employed the Arrhenius-type constitutive equations to investigate the effect of strain on hot deformation response of AA2124-T851 aluminum alloy at various strain rates. All the material constants were calculated at different strains. It was observed that all these the material constants varied with strain. The predicted flow stress values were compared to the measured ones and it was found that the maximum average absolute relative error (AARE) was 5.91 % which showed the good correlation between measured and predicted values. The AARE of 6.28 % was attained for the measured and predicted flow stress for AA7050 aluminum alloy [21].

2.4 High Strain Rate Deformation Behavior

Aluminum alloys are increasingly utilized in automotive and aviation industries due to their high strength-to-weight ratio. A large body of investigations focused on high strain rate deformation behavior of aluminum alloys, which enable engineers to modify the design of their products. For instance, data relating to the dynamic properties of these materials help engineers to design structural parts of an automobile to enhance their crash energy absorption capacity during collision [46]. A number of test procedures [47] such as impact test, drop weight test and Split Hopkinson pressure bar (SHPB) test have been used. Of these, the (SHPB) is widely used due to its accurate determination of stress-strain values at high strain rates [48]. One of the most reported failure mechanisms which occur during high strain rate deformation of metals is strain localization along adiabatic shear bands (ASBs) [49]. ASBs have been observed in specimens subjected to ballistic impact, explosive fragmentation, and high speed metal forming and manufacturing [50-52].

2.4.1 Properties of Adiabatic Shear Bands (ASBs)

Adiabatic shear bands (ASBs) are deformation zones in which high amount of strains are localized as a result of heterogeneous heat dissipation throughout the material under high strain rate condition. The majority of the kinetic energy produced in sever plastic deformation transforms to heat which accumulates in certain zones of the material than in the neighboring zone [53]. It was first suggested by Zener and Hollomon [39] that ASBs are formed within the material by thermal softening mechanism under high strain rate deformation condition.

A large number of theoretical and experimental investigations have been carried out to characterize the formation process and mechanical properties of ASBs [54-57]. To determine the formation process of localized shear bands, Costin et al. [58] developed the idea of estimating the temperature fluctuations in the narrow bands. Hartley et al. [59] and Marchand and Duffy [60] utilized an infrared technique to measure temperature oscillation and heat distribution during the deformation. They proposed that ASBs are formed in three steps. First, the stress waves are slightly inclined but still indicate homogenous deformation. Second, the stress wave lines are curved that shows inhomogeneous deformation occurrence. Third, the stress lines propagate discontinuously, which depicts of shear strain localization occurrence.

Recently, the concept of critical strain at which strain softening occurs has been extensively studied. It was found, that ASBs nucleate at the maximum point of stress- strain curves [61, 62]. The effect of heat treatment on the formation of localized shear strains in AISI 4340 steel was studied and it was observed that the critical strain was sensitive to thermal history [63]. Recht [64] found that there is a specific strain rate above which ASBs formation is triggered. Zurek [65] found that white etching bands in AISI 4340 were formed at both critical strain and strain rate, which were 0.5 and 1.8 10^4 s^{-1}, respectively. Lee et al [49] reported that shear stress and strain rate sensitivity of Al-Sc alloy were increased as strain rate increased. The width and hardness of the shear bands respectively decreased and increased with increasing deformation rate. Similar results were obtained in dynamic deformation of Al-Li alloy [66]. There were specific values of strain and strain rate at which either deformed or transformed shear bands formed. Deformed shear bands were observed in the alloy at a strain of 0.14 and a strain rate of 1600 s^{-1}. At higher strain values ($\varepsilon > 0.17$) white etching bands were formed in the peak aged alloy. Li et al. [67] investigated shear band formation in pure titanium alloy under shock loading

condition. Microstructural observations revealed that ASBs formed at critical strain and strain rate of 0.23, and 2800 s^{-1}, respectively.

2.4.2 Deformed Shear Bands and Transformed Shear Bands

Adiabatic shear bands (ASBs) are generally divided into two main groups, namely deformed shear bands (DSB) and transformed shear bands (TSB) based on their microstructural appearance [68]. Figure 2.3 shows DSBs which formed in an AA6061-T6 alloy under dynamic loading. Deformed shear bands form due to accumulation of more shear strain compared to the neighboring zones. Figure 2.4 shows TSBs which appear white under optical microscope [69]. The white etching bands existence has also been reported for steels under dynamic loading [39].

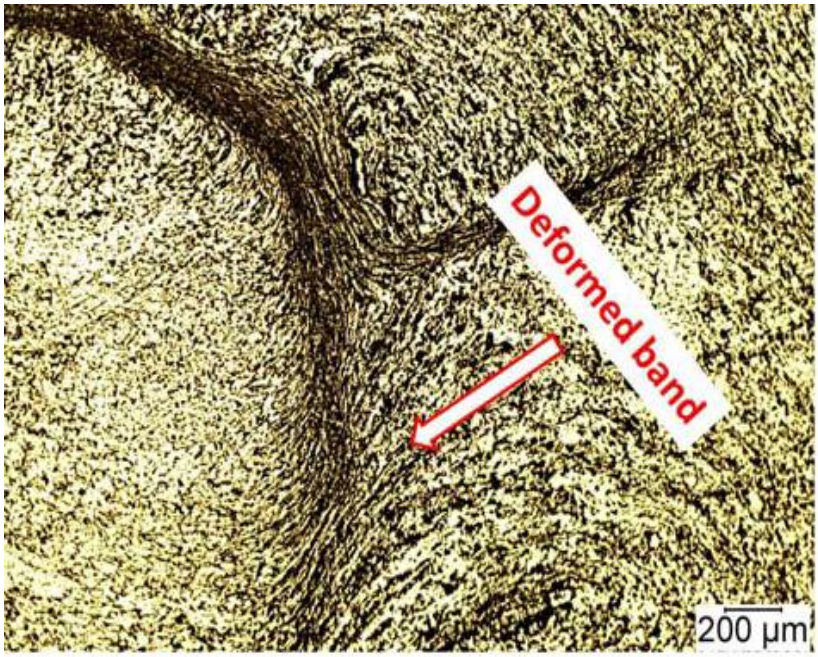

Figure 2.3. Optical micrograph of deformed shear band for AA6061-T6 alloy under dynamic loading [69].

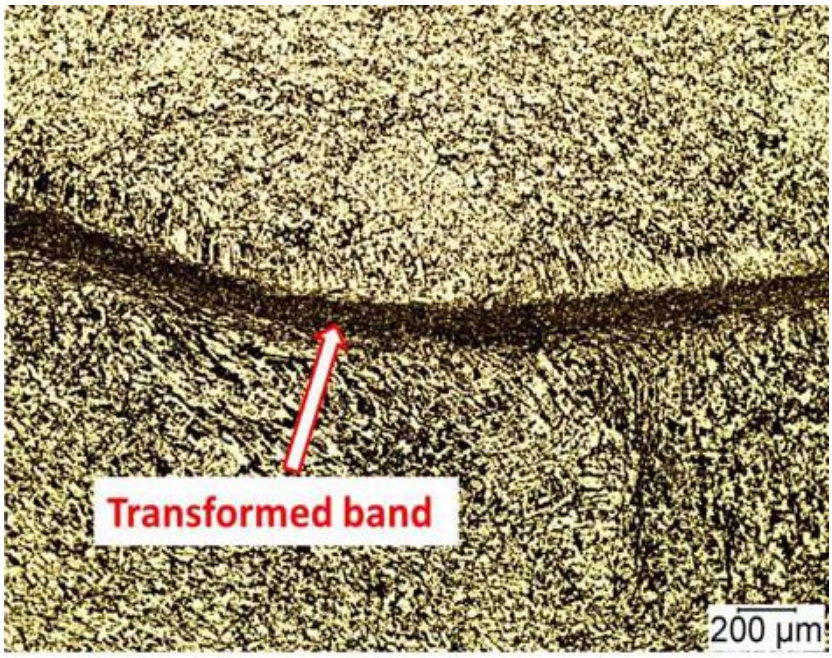

Figure 2.4. Optical micrograph of transformed shear band for AA6061-T6 alloy under dynamic loading [69].

Since FCC metals such as aluminum alloys are known as high stacking fault energy metals, they are less susceptible to form transformed shear bands [70, 71]. Microstructural examination of a cold rolled high purity aluminum which was compressed under high strain rate loading showed that there was no adiabatic shear band formation unless the degree of deformation approached 90% [72]. Textural softening was reported in FCC metals during cold rolling as a result of adiabatic shear band development throughout microstructure [73]. Adiabatic shear band formation has been reported in various kinds of aluminum alloy under shock loading [74-76].

Microstructural evaluation of Al-Li [66] alloy revealed that white etching band formation happened after the deformed shear band. Identification of white etching bands appears to be easy as apparently it has distinct white boundaries within bulk metal. To understand the formation process of white etching bands, a large number of researchers focused on the microstructural

changes in these shear bands under the dynamic loading. Zener and Hollomon [39] proposed that the white color of TSBs is a result of fast cooling from elevated temperatures.

2.4.3 The Effect of Initial Microstructure on ASBs Formation

The tendency for strain localization and adiabatic shear band formation under high strain loading is dependent on the alloy composition, heat treatment, and crystallographic orientation [74-77]. For example, Jia et al. [77] showed that development of adiabatic shear bands in FCC single crystals was affected by the original crystal orientation. It was reported that adiabatic shear band formation in Al-Mg alloys was influenced by magnesium content and crystallographic orientation [75]. An investigation of the tendency to strain localization in AA5059, AA5083, and AA7039 aluminum alloys showed that the possibility for ABS formation in 7039 aluminum alloy was the highest due to the presence of fine precipitates through the matrix [76]. In addition, transmission electron microscope (TEM) examination of edge and center parts of the shear bands in these aluminum alloys revealed intensely elongated dislocation cells and fine equi-axed grains, respectively. Shear strain localization was studied in equal channel angular (ECA) processed AA7075 aluminum alloy [78]. It was shown that the formation of ASBs was highly affected by the size of secondary phase precipitates.

Dynamic behavior of AA6061-T6, and AA5083-H131 under shock loading condition was compared [79]. It was demonstrated that the main dominant deformation mechanism was shear strain localization. The propensity to form ASBs in AA6061-T6 was found to be higher than AA5083-H131 due to the existence of secondary phases which act as preferential locations for nucleation of ASBs. While deformed shear bands were observed in AA5083-H131, white shear

bands were found in AA6061-T6 aluminum alloy. The effect of different tempers (e.g.,T4, T6 and T8) on microstructural characteristics and mechanical response of AA6061 and AA2099 under high strain rates was investigated by Odeshi et al. [80]. AA2099 showed the highest tendency to adiabatic shear strain failure in the T8 temper while AA6061 was more prone to strain localization failure in the T4 temper. Additionally, the pattern of crack propagation was found to be different in the two alloys. While a failure crack initiated and grew along the interface of shear band and bulk material in AA2099, it was propagated through the central line of white shear bands in AA6061. Al-Li alloy in four different heat treated conditions were deformed at various temperatures under high strain rate loading [66]. Although deformed and transformed shear bands were formed under all circumstances, the width and the length of the shear band varied under various thermal treatments and temperatures. It was reported that the propensity for crack initiation and propagation was higher at lower temperatures than at ambient temperatures [66].

2.5 Summary

A535 aluminum alloy shows potential applicability in fabricating different automobile parts such as engine blocks, pistons, cylinders and cylinder liners. Since there is little knowledge of its deformation behavior under elevated temperatures and high strain rates, quasi-static compression tests at elevated temperatures and shock loading tests of A535 aluminum alloy can be utilized to predict its deformation behavior under different strain rate and temperature conditions. This knowledge would be useful for selecting manufacturing processes and mechanical properties. Additionally, Arrhenius-type constitutive equations have been commonly used to find material constants such as n, n', A, A' and Q (activation energy) under hot deformation conditions. Finding these constant values for A535 aluminum alloy, especially activation energy (Q), can help to save energy and reduce manufacturing costs. The extended form of the Arrhenius equations have been used for different aluminum alloys to predict the flow stress behavior of the alloy at elevated temperatures and low strain rates.

CHAPTER 3

MATERIAL AND EXPERIMENTAL PROCEDURE

This chapter presents and discusses the experimental material and procedure used in this research. Two main mechanical tests were employed, namely: (i) hot compression test using a Gleeble^{TM} machine and (ii) dynamic shock loading test using a Split Hopkinson Pressure Bar (SHPB) apparatus. The method used to fit the obtained experimental data to constitutive equations is also presented.

3.1 Experimental Material

As-cast A535 aluminum alloy supplied by St. Paul Brass and Aluminum Foundry was used in this study. In accordance with ASTM E209 standards [81], the test specimens used for compression test were machined at Machine Shop located in Room 1B91, Engineering Building, University of Saskatchewan. The test specimens were machined in cylinders with diameter (D) of 6.5 mm and length (L) of 9.75 mm. A size ratio (i.e. L/D) of 1.5 was selected to prevent buckling during the deformation. The specimens used for dynamic shock loading test were prepared in accordance with ASTM E9 standards [82] as cylinders measuring 6.5 mm in diameter (D) and 7.25 mm in length (L) giving an L/D ratio of 1.1 (< 2) to ensure no buckling during testing. The chemical composition of the alloy was determined using an Inductively Coupled Plasma Mass Spectrometry (ICP-MS) (model: Perkim Elmer Nexlon 300 D-IG) located in Room 211, Department of Geological Science, University of Saskatchewan. The chemical composition of the alloy as obtained using the ICP-MS is shown in Table 3.1. The silicon (Si)

content of the alloy was undetectable by ICP-MS apparatus due to formation a volatile composition (SiF_4) within the digestion process of the alloy with Nitric acid (HNO_3) and Hydrofluoric acid (HF).

Table 3.1. Chemical composition of A535 aluminum alloy (wt. %).

Mg	Zn	Ca	Mn	Ti	Fe	Cu	Others
5.35	0.02	0.02	0.17	0.15	0.13	0.01	0.05

*Aluminum is the balance

3.2 Experimental Procedures

3.2.1 Heat Treatment of Test Specimens

To investigate the effect of heat treatment on mechanical behavior of A535 under various deformation conditions, a half of the specimens in accordance with American Society of Materials standard (ASM) were homogenized at 400˚C for five hours then quenched in water [10]. Heat treatment of A535 specimens was carried out using a Thermo Scientific™ Thermolyne™ furnace located in Room 2C24, Engineering Building.

3.2.2 Hot Compression Test

Hot compression test of A535 aluminum alloy was executed utilizing Gleeble™ 1500 machine (Figure 3.1), which was controlled by the QuickSim (version II) software. This test was performed at the Material Characterization Laboratory, University of Manitoba. Before testing,

all specimens had a K-type thermocouple soldered to the middle of the length, as shown in Figure 3.2. All specimens were held between apparatus anvils as shown in Figure 3.3 and heated at a rate of 10 K/s to the desired deformation temperature and held at this temperature for 10 seconds to attain uniform temperature throughout the specimen. After this stabilization, the specimen was compressed to 50% of its original length between the anvils of the Gleeble machine at a constant rate. The test temperatures used were 473 K, 573 K, 623 K and 673 K, while the strain rates used were 0.005 s^{-1}, 0.05 s^{-1}, 0.5 s^{-1} and 5 s^{-1}. When the compression was completed, the specimens were immediately quenched in water to preserve the resultant microstructure. For reproducibility, three specimens were tested for each deformation condition. Figure 3.4 shows a deformed specimen of A535 alloy after the compression test. All tested specimens indicated a slight degree of barreling, which is a result of the friction between the specimens' end surfaces and the anvils platens. Although the barreling occurrence was a sign of non-uniform deformation, the effect of that on the obtained stress-strain curves was neglected in the present research.

Figure 3.1. Picture of a Gleeble ™ 1500 machine.

During the compression test, all the data were recorded as load-displacement and engineering stress versus engineering strain values at 0.01 s intervals. By utilizing equations (3.1) and (3.2), the obtained engineering stress and engineering strain data were converted to true stress and true strain values, respectively, where σ_T is the true stress (MPa), ε_T is the true strain, σ_e is the engineering stress (MPa), and *e* is the engineering strain.

$$\sigma_T = \sigma_e \times (1+e) \tag{3.1}$$

$$\varepsilon_T = \ln(1+e) \tag{3.2}$$

As the compression test was progressed up to 50 percent reduction of its original length, these two equations were applied for the whole range of engineering stress and strain data. The

obtained data were then plotted as true stress versus true strain curves for the various deformation conditions.

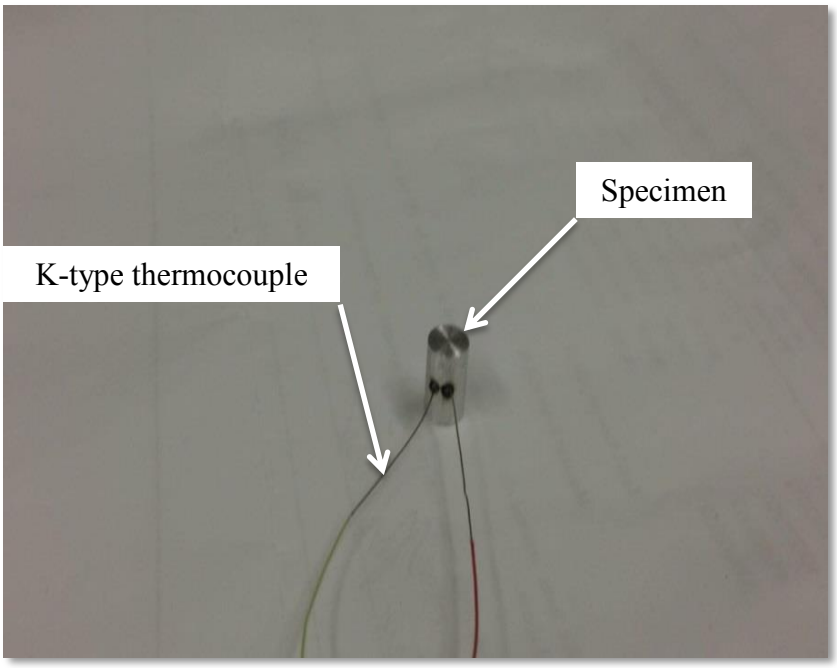

Figure 3.2. Picture showing how a K-type thermocouple was soldered to a specimen.

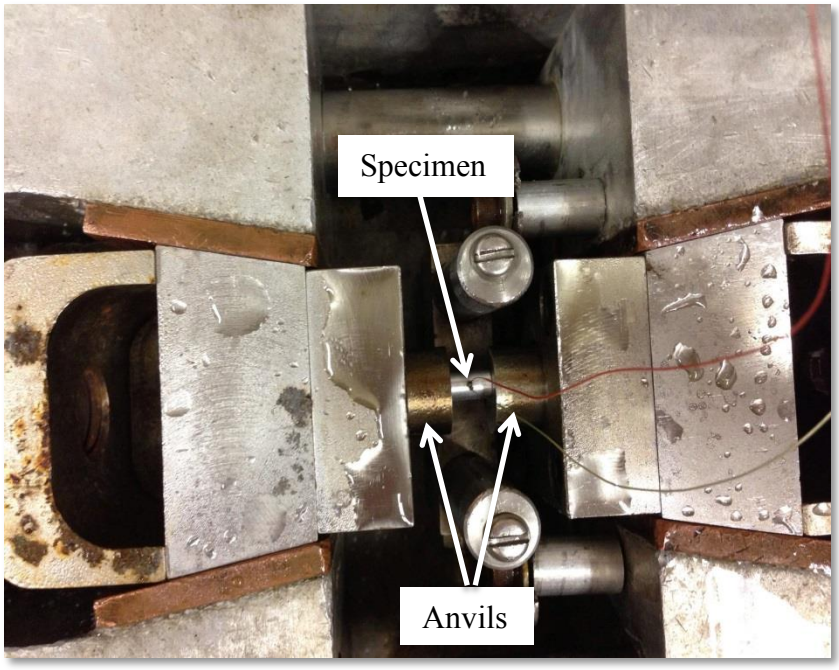

Figure 3.3. Picture showing how a specimen was held between anvils.

Figure 3.4. Picture of a barreled specimen of A535 alloy after compression test.

3.2.3 Fitting of Compression Test Experimental Data to Constitutive Equations

Constitutive equations are widely applied to describe the behavior of materials under various deformation conditions. Using constitutive equations yields some useful material property information such as strain rate sensitivity, strain, and temperature-flow stress dependence. One of the most frequently applied constitutive equations for hot deformation condition is the Arrhenius-type equation (equation (3.3)) [38], in which strain rate and temperature are related to flow stress (flow stress can be expressed in different forms of functions as shown in the equations (3.5) - (3.7)). Using equation (3.4), the simultaneous influence of strain rate and temperature can be represented by the Zener-Hollomon parameter (*Z* value) [39]. The flow stress can be expressed in different forms [83]: (i) power law (equation (3.5)), which breaks down at high stress level, (ii) exponential-type (equation (3.6)), which breaks down at low stress level, and (iii) hyperbolic sine (equation (3.7)), which is suitable for all ranges of stress. In these equations, $\dot{\varepsilon}$ (s^{-1}) = strain rate, σ (MPa) = flow stress, α (MPa^{-1}) = stress multiplier, *Q* (J mol^{-1}) = activation energy, *R* (8.31 J/mol.K) = universal gas constants, *Z* (s^{-1}) = Zener-Hollomon parameter, *T* (K) = absolute temperature, while *A* (s^{-1}), *A′* (s^{-1} MPa^{-1}), *A″* (s^{-1}), and *n* are material constants.

$$\dot{\varepsilon} = AF(\sigma)\exp\left(\frac{-Q}{RT}\right) \tag{3.3}$$

$$Z = \dot{\varepsilon}\exp\left(\frac{Q}{RT}\right) \tag{3.4}$$

$$\dot{\varepsilon} = A'\sigma^{n'}\exp\left(\frac{-Q}{RT}\right) \tag{3.5}$$

$$\dot{\varepsilon} = A'' \exp(\beta\sigma)\exp\left(\frac{-Q}{RT}\right) \tag{3.6}$$

$$\dot{\varepsilon} = A[\sinh(\alpha\sigma)]^n \exp\left(\frac{-Q}{RT}\right) \tag{3.7}$$

Taking the natural logarithm of both sides of equations (3.4) - (3.7) yields equations (3.8) - (3.11). From these equations, the flow stress values at a constant strain of 0.2 were extracted for various deformation conditions. Then, using equation (3.9), plots of ln[sinh(ασ)] against lnε̇ were made from which a group of parallel lines were obtained. The constant *n* was computed as the mean slope of those parallel lines. The same procedure was followed for equations (3.10) and (3.11) to calculate the material constants *n´* and β, respectively.

$$\ln Z = \ln \dot{\varepsilon} + \frac{Q}{RT} \tag{3.8}$$

$$\ln \dot{\varepsilon} = \ln A + n \ln[\sinh(\alpha\sigma)] - \frac{Q}{RT} \tag{3.9}$$

$$\ln \dot{\varepsilon} = \ln A' + n' \ln \sigma - \frac{Q}{RT} \tag{3.10}$$

$$\ln \dot{\varepsilon} = \ln A'' + \beta\sigma - \frac{Q}{RT} \tag{3.11}$$

The activation energy for deformation of A535 aluminum alloy was calculated using equation (3.12). *S* is the mean slope of the parallel lines obtained by plotting ln[sinh(ασ)] versus 1/*T* at constant strain rates. By substituting calculated *S* and *n* in the equation (3.12), the activation energy (*Q*) at a constant strain was obtained under different deformation conditions. The obtained activation energy values were substituted in equation (3.13) to calculate the value of material constant *A* as shown in equation (3.14). The same procedure was followed for

calculating constant A' and A'' using equations (3.10) and (3.11), respectively. Eventually, by substituting the obtained activation energy into to equation (3.4), the Zener-Hollomon parameter was calculated for various deformation conditions.

$$Q = R\left[\frac{\partial \ln \dot{\varepsilon}}{\partial \ln(\sinh \alpha\sigma)}\right]_T \times \left[\frac{\partial \ln(\sinh \alpha\sigma)}{\partial(\frac{1}{T})}\right]_{\dot{\varepsilon}} = RnS \tag{3.12}$$

$$\ln[\sinh \alpha\sigma] = \frac{1}{n}\ln \dot{\varepsilon} - \frac{1}{n}\ln A + \frac{Q}{nRT} \tag{3.13}$$

$$Intercept = \frac{1}{n}\ln \dot{\varepsilon} - \frac{1}{n}\ln A \tag{3.14}$$

It can be deduced from equation (3.3) that the effects of the deformation temperature and the strain rate on the flow stress are considered, whereas the effect of strain can be ignored. Thus, to investigate the impact of strain on the mechanical behavior of A535 aluminum alloy, flow stress values at various strains in the range of 0.05 to 0.4 were selected at 0.05 intervals. Then, all the material constants such as n, n', A, A', A'', and Q were individually calculated at each strain. In order to determine the influence of strain on the material constants, each of the obtained constants was plotted separately against strain. By utilizing Sigmaplot™ software package (Version 11), curves of fifth order polynomial were fitted to all material constants curves to obtain a function of the variation of each material constant with strain. Finally, by using equations (3.4) - (3.7), all material constants were calculated at different strains. Computed activation energies were substituted into the Zener-Hollomon parameter equation to determine the Z values for various strains. After calculating all material constants, the flow stress values were predicted under different deformation conditions using equation (3.15). Thus, by utilizing the extended form of the constitutive equations it is possible to predict the flow stress values

under diverse deformation circumstances. Equation (3.16) [45] shows the relative error formula by which predicted values could be verified with the experimental results. In this equation σ_M (MPa) is the measured stress and σ_C (MPa) is the calculated stress.

$$\sigma = \frac{1}{\alpha}\ln\left\{\left(\frac{Z}{A}\right)^{\frac{1}{n}} + \left[\left(\frac{Z}{A}\right)^{\frac{2}{n}} + 1\right]^{\frac{1}{2}}\right\} \tag{3.15}$$

$$\text{Relative Error} = \frac{|\sigma_C| - |\sigma_M|}{|\sigma_M|} \times 100\% \tag{3.16}$$

3.2.4 Dynamic Shock Loading

To evaluate how A535 aluminum alloy responds to shock loading, compression test was conducted at high strain rates and room temperature using a Split Hopkinson Pressure Bar (SHPB) apparatus, which is located in Room 2C24, Engineering Building. A535 aluminum alloy specimens were tested in as-cast and homogenized conditions. The SHPB apparatus is shown in Figure 3.5. It consists of a gas gun (or a launching device), a strike bar, an incident bar which is made of maraging steel with a diameter of 38 mm, a transmission bar, an energy absorption device and a computerized data acquisition system.

The specimen was held between the incident bar and the transmission bar. Since friction between the specimen ends and the bar interface can cause a heterogeneous stress wave distribution through the specimen (buckling), the two end surfaces of the specimens were lubricated with Vaseline to minimize friction. After mounting the specimens, the strike bar was fired by a

compressed gas gun and traveled through the gun barrel to strike the end of the incident bar. The elastic wave generated was transmitted through the incident bar to the specimen. The wave transmitted through the incident bar was captured by the strain gage attached to the bar as incident wave. Part of the incident wave was utilized in deforming the specimen, while the other was reflected back at the specimen-incident bar contact surface and captured by the strain gage mounted on the incident bar as reflected wave. Part of the incident wave transmitted through the specimen was captured by the strain gage on the transmitter bar as transmitted wave. The signals of incident, reflected, and transmitted waves were conditioned and amplified by the connected signal conditioner and captured by a mixed signal digital oscilloscope. Since the sensors (strain gages) were attached to the bars, it was important to ensure that the strength of incident and transmitter bars was higher than that of the specimen in order for the deformation of the bars to remain elastic during the whole deformation. Additionally, it was important to place the specimen between the bars parallel to both incident and transmitted bars to promote a uniaxial stress.

The incident bar was impacted by the strike bar to yield strain rates of 1400 s^{-1}, 1600 s^{-1}, 1800 s^{-1}, 2000 s^{-1}, 2200 s^{-1} and 2400 s^{-1} in the A535 specimens at ambient temperature. To ensure reproducibility the three specimens were tested for the same strain rate. The obtained data were saved as time versus voltage (see a typical graph in Figure 3.6) and later converted to engineering strain rate, engineering strain and engineering stress utilizing equations (3.17), (3.18) and (3.19), respectively [84].

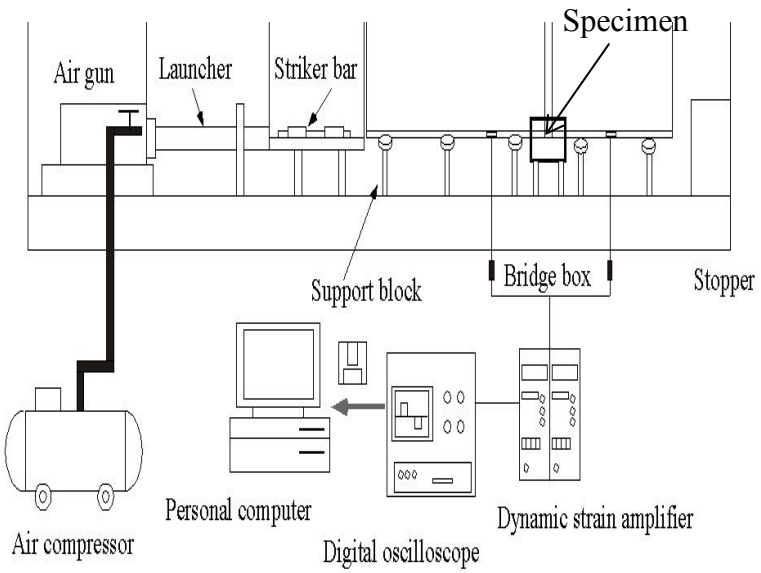

Figure 3.5. Schematic of a split Hopkinson pressure bar (SHPB) apparatus.

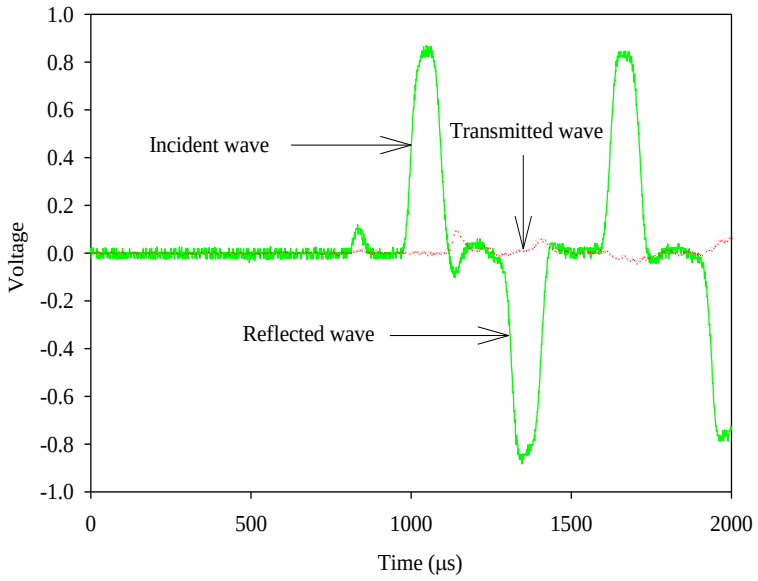

Figure 3.6. Typical voltage-time graph of dynamic load test of A535 aluminum alloy.

$$\dot{\varepsilon} = -2\frac{C_B}{L_S}\varepsilon_R \tag{3.17}$$

$$\varepsilon = -2\frac{C_B}{L_S}\int_0^t \varepsilon_R dt \tag{3.18}$$

$$\sigma = \frac{A_B}{A_S}E_B\varepsilon_T \tag{3.19}$$

where, $\dot{\varepsilon}$ = engineering strain rate (s^{-1}), ε = engineering strain, σ (MPa) = engineering stress, C_B = velocity of sound in the incident bar (4581 m/s), L_s = sample length (m), ε_R = reflected strain, ε_T = transmitted strain, A_B (mm^2) = cross sectional area of the bar, A_s (mm^2) = cross sectional area of the specimen and E_B is the elastic modulus of the incident bar (185 GPa).

3.2.5 Metallographic Examination

As-cast and homogenized A535 aluminum alloy specimens used for shock loading test were cut by a precision cutter (BUEHLER ISOMET) equipped with a diamond saw with the diameter of 12.33 mm and thickness of 0.4 mm parallel to the load direction (longitudinal direction). To prevent any microstructural alteration because of temperature rise during cutting, oil coolant was used to lubricate the interface of saw and specimen. Specimens were subsequently hot-mounted in epoxy molds using a LECO PR-22 apparatus. After mounting, the specimens were ground and polished using 240-grit a (SiC) paper, 9 µm diamond paste, 3 µm diamond paste and oxide polishing-suspension (OP-S) colloidal silica in that order [85]. They were finally cleaned in distilled water following cleaning in methanol and dried before etching. Etching of the specimens was carried out using the Keller's reagent, which consisted of 95ml H_2O, 2.5ml HNO_3, 1.5ml HCl and 1ml HF [85]. The etched specimens were examined in a metallurgical

optical microscope (NIKON MA 100) and electron microscope (JEOL JSM-6010LV), located in Room 2C25, Engineering Building, to understand the microstructures developed during deformation.

3.3 Summary

As-cast and homogenized A535 specimens were compressed using a Gleeble^{TM} machine at temperatures of 473 K, 573 K, 623 K and 673 K and strain rates of 0.005 s^{-1}, 0.05 s^{-1}, 0.5 s^{-1} and 5 s^{-1}. The experimental data were fitted to the Arrhenius-type equation to determine material constants and *Z* values for A535 alloy under different deformation conditions. The Arrhenius equation was extended to evaluate the effect of strain on A535 constants and predict the flow stress under various deformation conditions. In addition, the mechanical response of as-cast and homogenized A535 under high strain rate deformation condition was investigated at room temperature using a SHPB machine at strain rates of 1400 s^{-1}, 1600 s^{-1}, 1800 s^{-1}, 2000 s^{-1}, 2200 s^{-1}, and 2400 s^{-1}. The microstructures of the specimens obtained after hot deformation and shock loading compression were examined using optical microscope (OM) and scanning electron microscope (SEM).

CHAPTER 4

RESULTS AND DISCUSSIONS

In this chapter experimental and numerical results obtained following the program described in Chapter 3 are reported and analyzed. The results presented cover the two experiments carried out as described in Chapter 3, namely: (i) deformation of A535 aluminum alloy at the elevated temperatures and low strain rates (quasi-static loading) and (ii) high strain rate (shock loading) deformation of A535 aluminum alloy.

4.1 Hot Deformation Behavior of A535 Aluminum Alloy

4.1.1 True Stress-Strain Curves Analysis

Figure 4.1 (a) - (d) shows true stress-true strain curves obtained for as-cast A535 aluminum alloy at different strain rates using the hot compression test. Figures 4.2 (a) - (d) show similar results obtained for specimens of A535 homogenized at 450˚C for 5 hours to determine the effect of heat treatment on the deformation behavior of the alloy. The overall shape of all stress-strain curves in Figures 4.1 and 4.2 is similar. The flow stress in both cases initially increased sharply up to a certain level of strain (0.03) after which it increased gradually with increasing strain. However, above approximately 0.3 true strain the flow stress started to increase at a higher rate than it did between 0.03 and 0.3. This continued until the end of deformation. A close examination of the stress-strain curves shows that the flow stress of A535 aluminum alloy is sensitive to both temperature and strain rate; it increased with increasing strain rate but decreased with increasing temperature. The initial rapid increase in strain hardening rate observed in

Figures 4.1 and 4.2 could be attributed to resistance due to dislocation multiplication, enhancement of dislocation strain field interactions and dislocation tangling.

Between 0.03 and 0.3 strain, the rate of strain hardening remained virtually constant, which is thought to be due to softening activities that balanced strain hardening. At strains higher than 0.3, strain hardening rate increased (though not as rapidly as in the initial stage) due to less time for restoration mechanisms of dynamic recovery (DRV) and dynamic recrystallization (DRX).

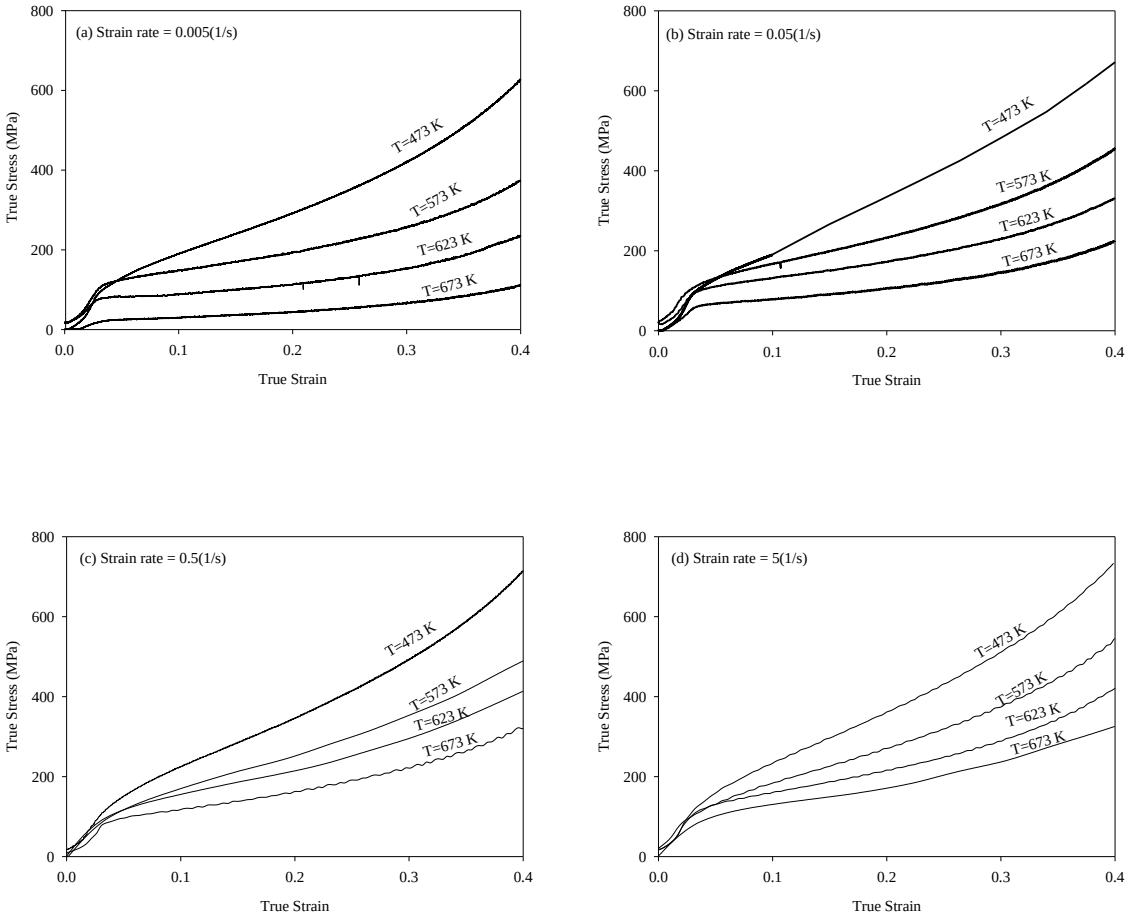

Figure 4.1. Representative true stress-true strain curves obtained for as-cast A535 aluminum alloy at different strain rates: (a) 0.005 s^{-1}, (b) 0.05 s^{-1}, (c) 0.5 s^{-1} and (d) 5 s^{-1}.

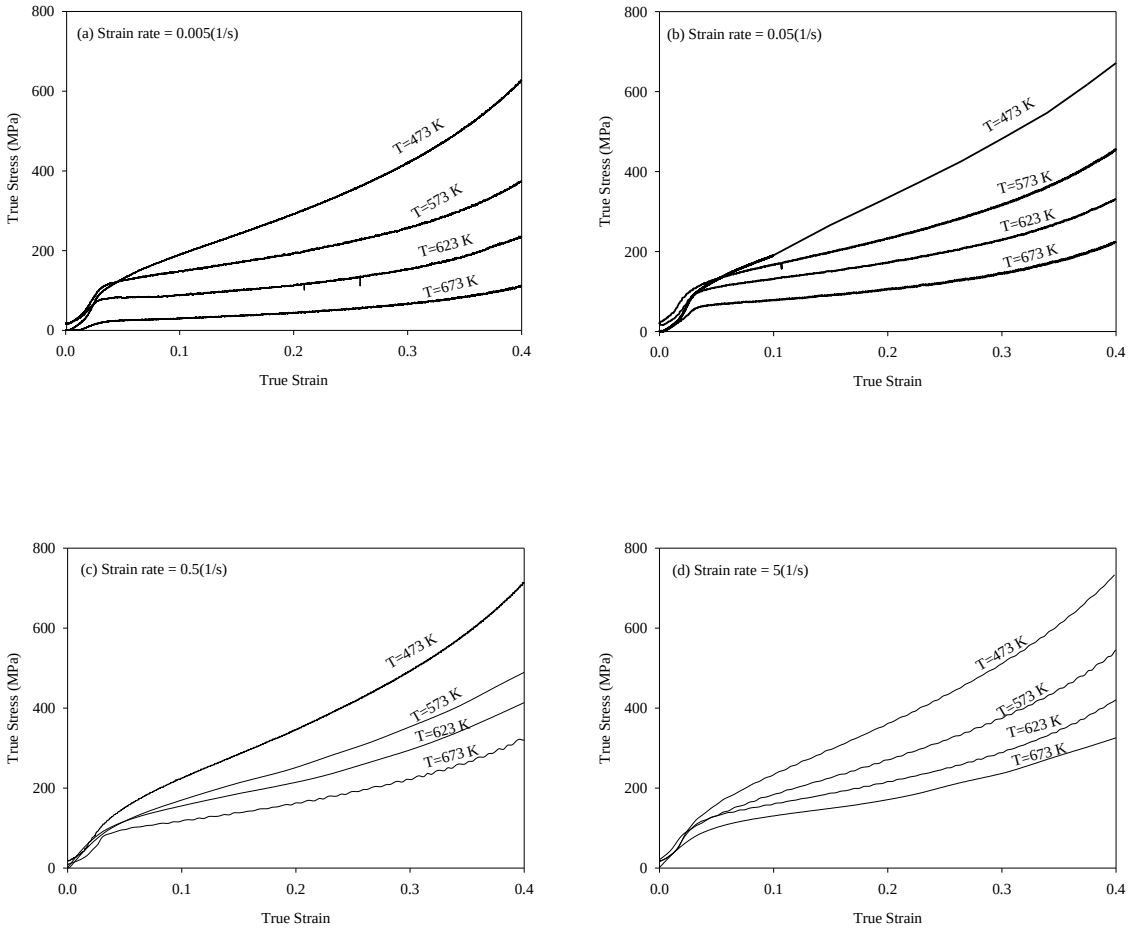

Figure 4.2. Representative true stress-true strain curves obtained for homogenized A535 aluminum alloy at different strain rates: (a) 0.005 s^{-1}, (b) 0.05 s^{-1}, (c) 0.5 s^{-1} and (d) 5 s^{-1}.

Aluminum alloys exhibit two types of stress-strain trends after the transition point under hot compression deformation conditions. In the first case, the flow stress remains steady or decreases with increasing strain, which is an indication of activation of softening mechanisms. In the second type, the flow stress exhibits continuous rise, which is an indication of further work hardening after attaining the peak [16]. Lou et al. [34] reported a decline in flow stress after the initial peak for Al-Zn-Mg-Cu alloy under hot deformation conditions. Microstructural examinations of their specimen suggested that DRV mainly conrolled the deformation of this alloy. Similar stress-strain curves were obtained for AA2026 [86], Al-Cu-Mg [43], AA2124-

T851[45], Al-5.7 wt.%Mg-Er [31], Al-Mg-Si-Cu [33], AA2219 [30] and AA7150 [18] aluminum alloys under high temperture deformation. J.Li et al. [21] reported further strain hardening after the initial peak for AA7050 aluminum alloy under hot deformation conditions. However, the rate of strain hardening was different for various deformation conditions. Similar post-initial peak strain hardening was observed for A357 [22], A356 [23], AA5052 [24], AA5182 [25] and AA1070 [87] at elevated high temperatures. The stress-strain curves obtained for as-cast and homogenized A535 alloy in the present study are consistent with these results (i.e. Refs [21-25, 87]).

Ebrahimi et al. [26] studied the deformation behavior of AA2024 aluminum alloy under quasi-static loading after solution heat treatment and annealing. It was observed that the flow stress curves obtained for supersaturated specimens were higher than their counterparts for annealed specimens. The amount of work softening for the supersaturated specimens was much higher than the annealed ones. This was attributed to the dynamic nucleation and growth of precipitates which reduced their ability against dislocations motions. Similar results were reported for homogenized and solution treated AA7085 [27], AA6082 [28], AA6201 [29], and AA2219 [30] aluminum alloys under quasi-static test loading. The softening observed in the aforementioned solution heat treated aluminum alloys was attributed to coarsening of precipitates formed during dynamic precipitation (DPN). Nucleation of precipitates impedes dislocation motion, which increases the peak stress level. However, at low strain rate these precipitates grow, which decrease their ability to lock mobile dislocations. In this regard, coarsening of dynamically precipitated phase accounted for higher rate of dynamic softening of solutionized samples than the annealed ones at lower temperatures. Although heat treatment was found to be an effective parameter on deformation behavior of different aluminum alloys, the obtained stress-strain

curves for A535 alloy showed that heat treatment has no effect on the mechanical response of the alloy under the hot deformation conditions.

4.1.2 Constitutive Analysis

Arrhenius-type equations are frequently used to model material behavior under hot deformation conditions. In order to analyze the influence of strain rate and deformation temperature on the deformation behavior of A535 aluminum alloy, the stress values were extracted at a strain of 0.2. This point was chosen because it falls within the region where flow stress attained a steady state under various deformation conditions.

Figure 4.3 shows the plot of natural logarithm of strain rate ($\ln\dot{\varepsilon}$) versus natural logarithm of $\sinh(\alpha\sigma)$ obtained for as-cast specimens of A535 alloy under various deformation temperatures. By applying linear regression to equation (4.1) for each line and calculating the mean value of all obtained slopes, the parameter *n* was calculated, which is 3.3. α is a stress multiplier, which was determined by trial and error to fit each set of stress data with the best straight line (i.e, lines with highest *R* squared). At a strain of 0.2, the best estimated value of α was found to be 0.022 MPa^{-1}.

$$\dot{\varepsilon} = A[\sinh(\alpha\sigma)]^n \exp\left(\frac{-Q}{RT}\right) \tag{4.1}$$

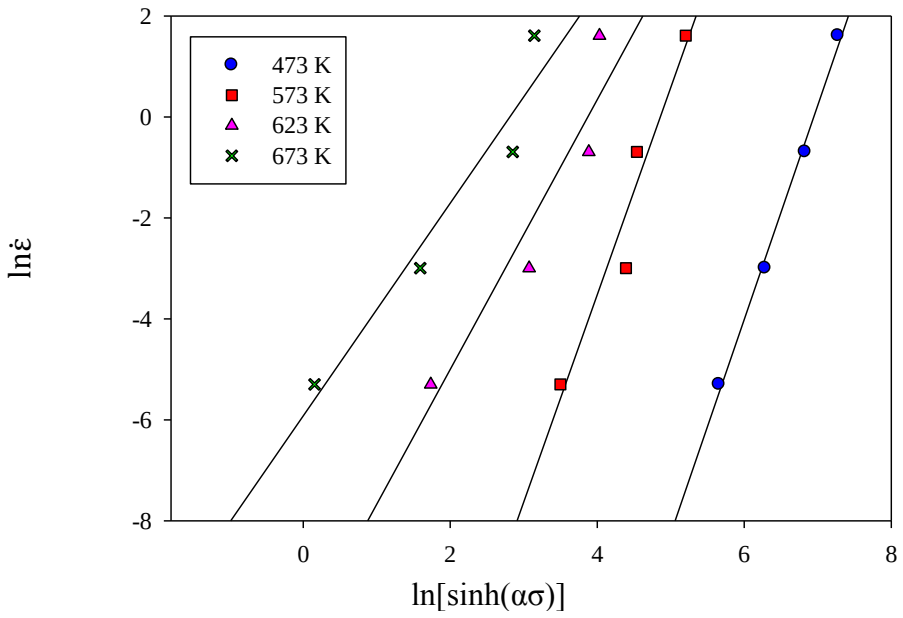

Figure 4.3. Variation of ln[sinh(ασ)] with lnε̇ for as-cast A535 alloy under different deformation conditions.

It can be seen from Figure 4.3 (the same graph obtained for homogenized specimens of A535 alloy) that the slope of the fitted straight lines varied with the deformation temperature. Hence, by increasing the deformation temperature from 473 K to 673 K the slopes of the lines (n) decreased from 4.24 to 2.1. As such it can also be concluded that the effect of strain rate on flow stress was more pronounced at lower temperatures. Figure 4.4 (the same graph obtained for homogenized specimens of A535 alloy) shows the variation of lnε̇ versus lnσ for as-cast A535 alloy, which was obtained by taking natural logarithm of equation (4.2); where A' ($s^{-1}\,MPa^{-1}$) and n' are material constants. In accordance with equation (4.2), the average of the slope of the fitted straight lines yielded material constant n' as shown in Figures 4.4 for as-cast A535 alloy. Figure 4.5 (the same graph obtained for homogenized specimens of A535 alloy) shows the variation of lnε̇ against flow stress (σ) for as-cast A535 alloy, which was obtained by taking natural logarithm of equation (4.3); where A'' (s^{-1}) and β are material constants. The material constant β

was calculated for as-cast and homogenized A535 alloy through linear regressions of fitted straight lines in Figure 4.5.

$$\dot{\varepsilon} = A'\sigma^{n'} \exp\left(\frac{-Q}{RT}\right) \tag{4.2}$$

$$\dot{\varepsilon} = A'' \exp(\beta\sigma)\exp\left(\frac{-Q}{RT}\right) \tag{4.3}$$

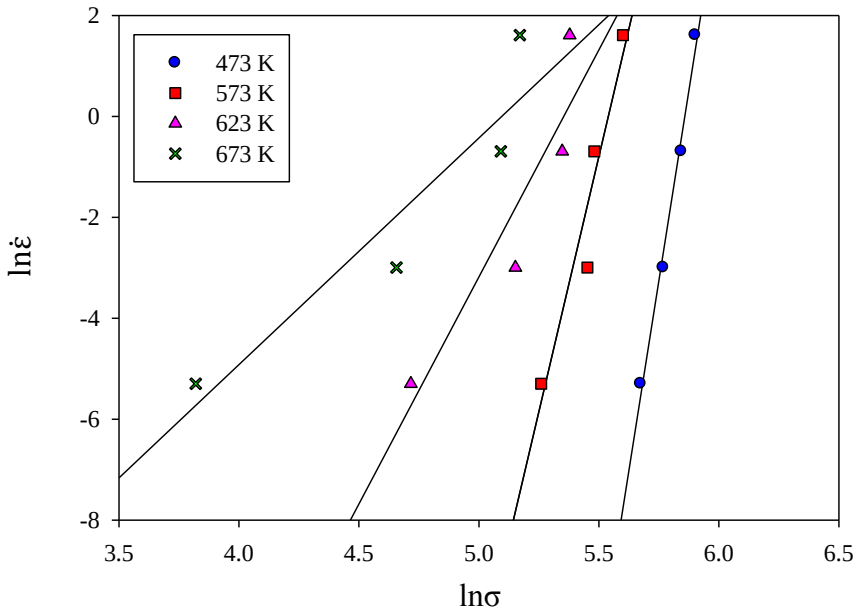

Figure 4.4. Variation of lnσ with lnε̇ obtained for as-cast A535 alloy.

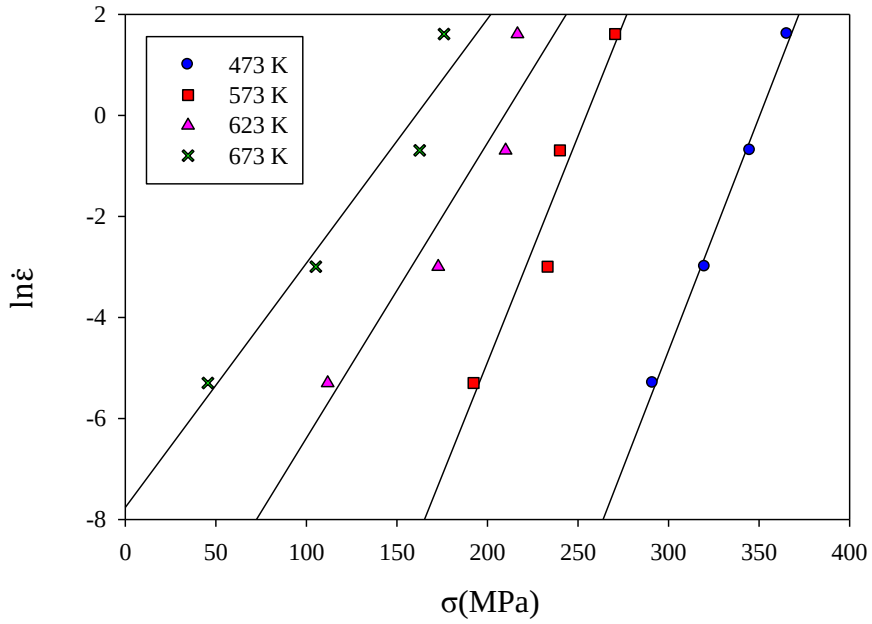

Figure 4.5. Variation of σ with lnε̇ obtained for as-cast A535 alloy.

Figure 4.6 (the same graph obtained for homogenized specimens of A535 alloy) shows the variation of ln[sinh(ασ)] with 1000/T (K^{-1}), which was obtained by differentiating equation (4.1) to get equation (4.4); where R (8.31 J/mol.K) is universal gas constant, n and S (K) are material constants. The activation energy for the A535 aluminum alloy was calculated by substituting the average slopes of fitted straight lines (S) as shown in Figure 4.6 and in equation (4.4). The activation energy for as-cast and homogenized A535 alloy was calculated to be 193 kJ/mol. The material constant A was also calculated by substituting the intercepts of the lines of Figure 4.6, and substituting in equation (4.5) which is derived from equation (4.1). The calculated material constants with their standard deviations are listed in Table 4.1 (the same results obtained for homogenized specimens of A535 alloy) for as-cast A535 alloy.

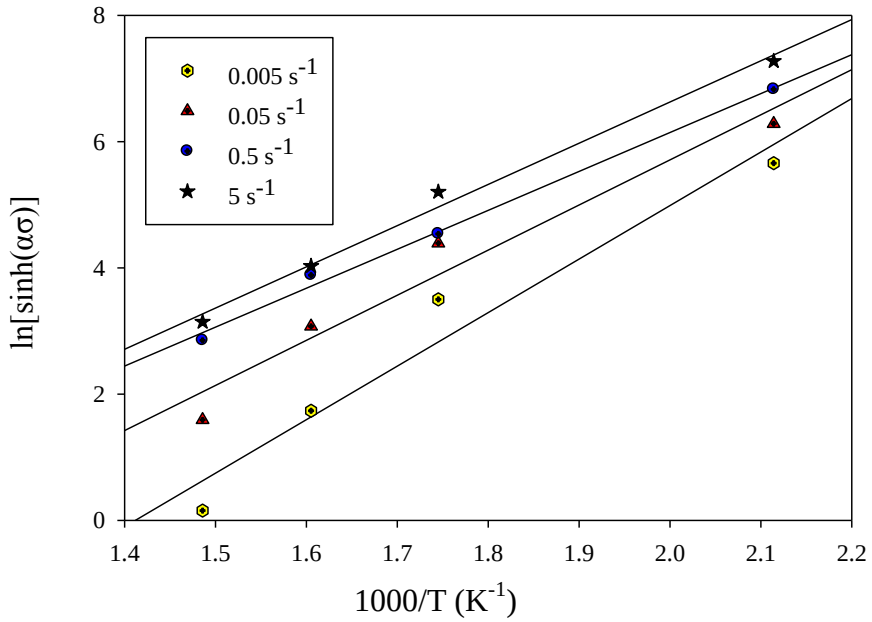

Figure 4.6. Variation of ln[sinh(ασ)] with 1000/T (K^{-1}) obtained for as-cast A535 alloy at different strain rates.

$$Q = R\left[\frac{\partial \ln \dot{\varepsilon}}{\partial \ln(\sinh \alpha\sigma)}\right]_T \times \left[\frac{\partial \ln(\sinh \alpha\sigma)}{\partial(\frac{1}{T})}\right]_{\dot{\varepsilon}} = RnS \tag{4.4}$$

$$\ln A = \ln \dot{\varepsilon} - (n \times Intercept) \tag{4.5}$$

Table 4.1. Calculated material constants for as-cast A535 aluminum alloy at the true strain of 0.2.

n	*n´*	β (MPa^{-1})	*lnA*	α (MPa^{-1})	*Q* (kJ/mol)
3.3 ± 0.9	15.95 ± 3.94	0.072 ± 0.004	25.35 ± 3.64	0.022	193 ± 14.8

Activation energy is a physical characteristic of a material which indicates the severity of plastic deformation [18]. Different aluminum alloys possess various levels of activation energy, which is affected by factors such as deformation conditions, composition of the alloy, manufacturing process and heat treatment [34]. The obtained activation energy for as-cast and homogenized A535 (Q = 193 kJ/mol) is higher than the activation energy for self-diffusion of pure aluminum (Q = 142 kJ/mol) [41, 88] due to occurrence different phenomena during deformation such as dislocation tangling, dislocation slipping and diffusion of voids and solute atoms. Different values of activation energy were reported for deformation of Al-Mg alloys due to variation of alloying content specifically magnesium, and assuming different values for α (stress multiplier) in the calculations. McQueen et al. [38] compared a wide range of activation energies for deformation of Al-Mg alloys, which varied in the range of 145-218 kJ/mol. Activation energy for deformation of AA5083 [89] aluminum alloy with magnesium contents of 4.4 and 5.2 (wt.%) was reported to be 185 and 178 kJ/mol, respectively. Obtained activation energy for deformation of as-cast and homogenized A535 alloy (Q = 193 kJ/mol) is close to those reported for AA5083 aluminum alloy.

The Zener-Hollomon relationship of equation (4.6) was rewritten for A535 aluminum by introducing the calculated activation energy to yield equation (4.7). In addition, by using the hyperbolic sine equation and Zener-Hollomon parameter equation (i.e. equations (4.1) and (4.6)), the flow stress can be related to the Zener-Hollomon parameter as shown in equation (4.8). Flow stress values can then be predicted for a given true strain, say 0.2 by utilizing equation (4.9), which was obtained by substituting calculated material constants (α, A and n) into equation (4.8).

$$Z = \dot{\varepsilon} \exp\left(\frac{Q}{RT}\right) \tag{4.6}$$

$$Z = \dot{\varepsilon} \exp\left(\frac{193 \times 10^3}{8.314 \times T}\right) \tag{4.7}$$

$$\sigma = \frac{1}{\alpha} \ln\left\{\left(\frac{Z}{A}\right)^{\frac{1}{n}} + \left[\left(\frac{Z}{A}\right)^{\frac{2}{n}} + 1\right]^{\frac{1}{2}}\right\} \tag{4.8}$$

$$\sigma = \frac{1}{0.022} \ln\left\{\left(\frac{Z}{1.025 \times 10^{11}}\right)^{\frac{1}{3.3}} + \left[\left(\frac{Z}{1.025 \times 10^{11}}\right)^{\frac{2}{3.3}} + 1\right]^{\frac{1}{2}}\right\} \tag{4. 9}$$

Table 4.2 shows the natural logarithm values of Zener-Hollomon parameters (*Z* values) obtained for as-cast A535 alloy (the same results obtained for homogenized specimens of A535 alloy) under different deformation conditions using equation (4.7). It can be seen that *Z* values are increased with increasing strain rate and decreasing deformation temperature. Similar results observed for calculated *Z* values for AA2026 [86] and AA7150 [18] aluminum alloys.

Table 4.2. Natural logarithm values of the Zener-Hollomon parameter obtained for as-cast A535 alloy under various deformation conditions.

Strain rate (s^{-1}) →	0.005	0.05	0.5	5
Temperature (K) ↓				
473	43.8	46	48.4	50.7
573	35.22	37.53	39.83	42.13
623	32	34.3	36.6	38.9
673	29.2	31.5	33.8	36.11

4.1.3 Strain Rate Sensitivity

Strain rate and flow stress are related as shown in equation (4.10), where *C* (MPa s) is a material constant and *m* is strain rate sensitivity coefficient. Strain rate sensitivity is an index which shows the variation of flow stress with strain rate. By taking the natural logarithm of both sides of equation (4.10) and plotting the natural logarithm of flow stress versus natural logarithm of strain rate, as shown in Figure 4.7 (the same graph obtained for homogenized specimens of A535 alloy), a series of linear regressions were obtained from which *m* was computed. The obtained values of *m* for as-cast and homogenized A535 alloy at the true strain of 0.2 are shown in Table 4.3 (the same results obtained for homogenized specimens of A535 alloy).

$$\sigma = C\dot{\varepsilon}^{m} \tag{4.10}$$

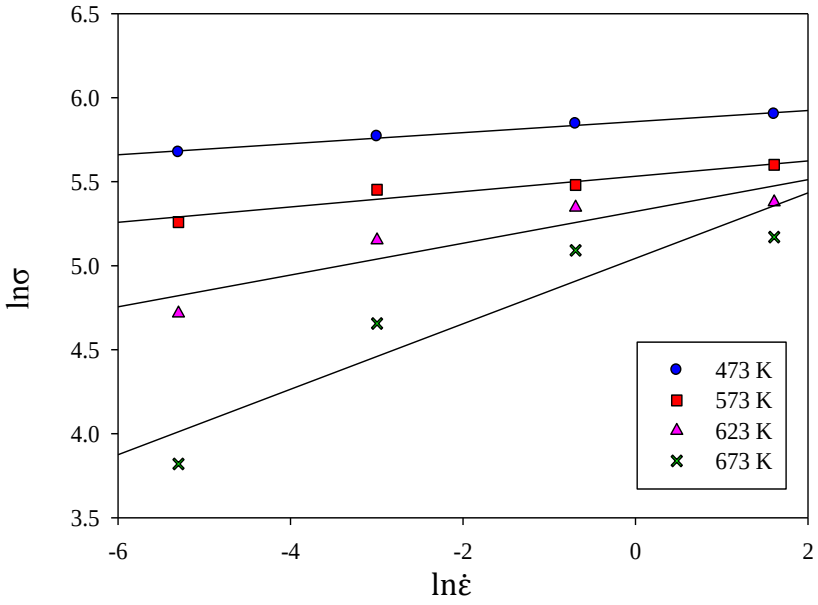

Figure 4.7. Variation of lnσ with lnε̇ for as-cast A535 alloy at different temperatures.

Table 4.3. Calculated strain rate sensitivity (*m*) at different temperatures at a true strain of 0.2 for as-cast A535 alloy.

	Temperature (K)			
Specimen condition	473	573	623	673
As-cast	0.03	0.05	0.09	0.19

The strain rate sensitivity of A535 aluminum alloy increased substantially with increasing deformation temperature. This means that at higher temperatures an increase in strain will need more stress to perform the same degree of deformation than that at lower temperatures, at the same strain rate.

4.1.4 Constitutive Analysis Considering Compensation of Strain

In the Arrhenius constitutive equations, the effect of the strain rate and deformation temperature were considered in the prediction of material constants while the effect of strain on mechanical behavior of material was completely ignored. A number of studies have utilized extended constitutive equations through various strains to calculate all material constants (i.e. n, n', α, β, A, Q) to consider the effect of strain on the deformation behavior of material. By plotting calculated material constants versus strain, a function of strain can be found by finding the best fit curve to all calculated values. By utilizing equation (4.6), Zener-Hollomon parameter (Z value) can be calculated under different deformation conditions and strains by substituting calculated activation energy values (Q) for various strains. Then, these calculated Z values and material constants (i.e. α, A and n) can be substituted in equation (4.8) to predict the flow stress for various strains under different deformation conditions.

The strain compensation effect has been investigated for various types of aluminum alloys under hot deformation conditions. In order to investigate the effect of strain on the mechanical response of A535 aluminum alloy at elevated temperatures, flow stress values were selected at different true strains ranging from 0.05 to 0.4 at 0.05 intervals under different deformation conditions. All material constants were calculated individually at each strain point following the procedure used for the single strain of $\varepsilon = 0.2$. Figures 4.8 to 4.13 (the same graphs were obtained for homogenized specimens of A535 alloy) show the variation of the calculated material constants with true strain for as-cast and homogenized A535 alloy compressed at elevated temperatures. The error bars represent standard error of each material constant at different strains.

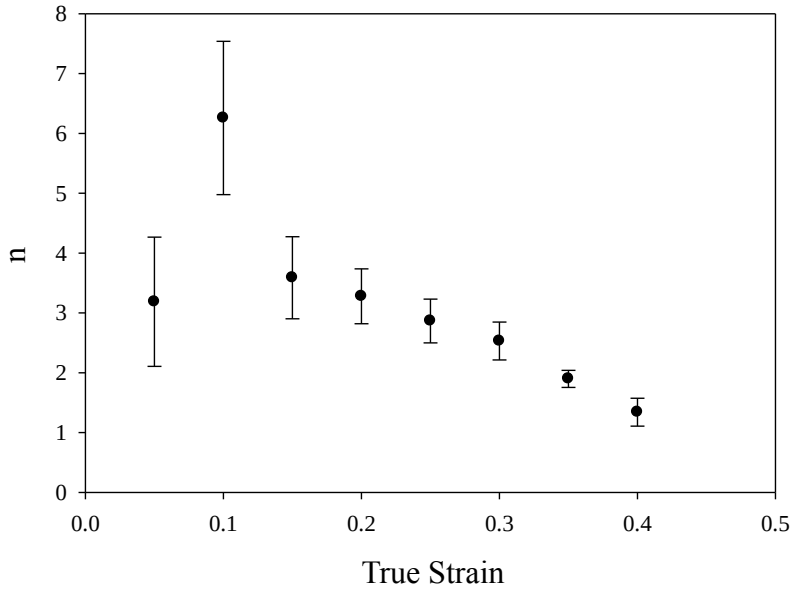

Figure 4.8. Variation of *n* with strain for as-cast A535 alloy.

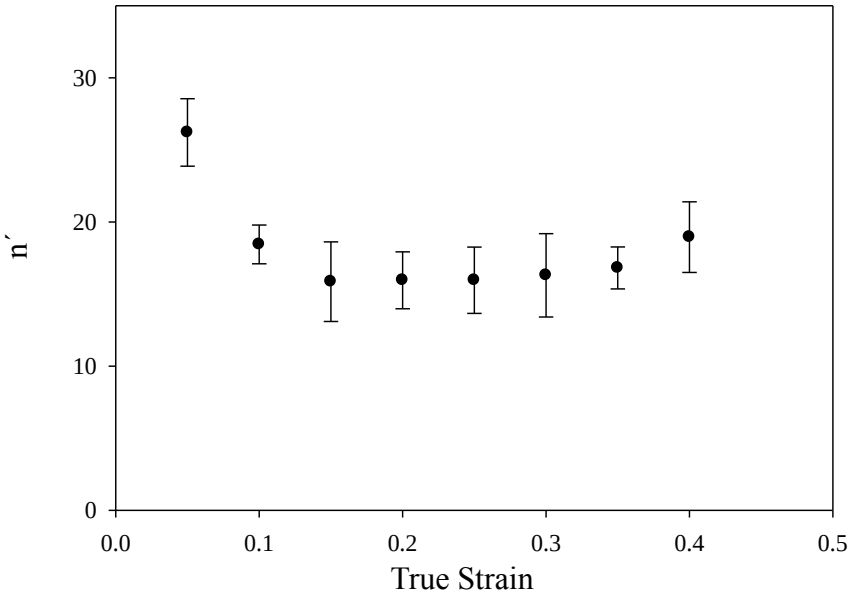

Figure 4.9. Variation of *n´* with strain for as-cast A535 alloy.

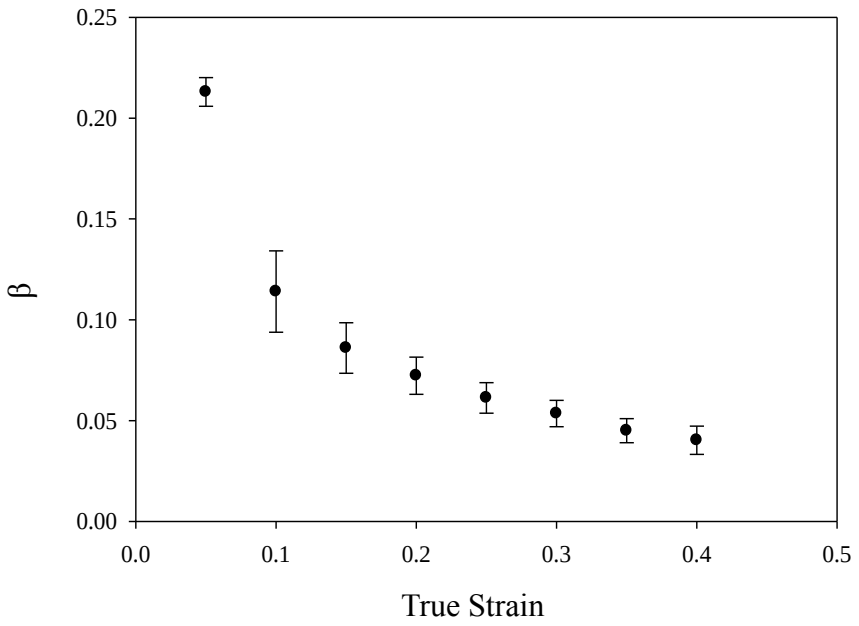

Figure 4.10. Variation of β with strain for as-cast A535 alloy.

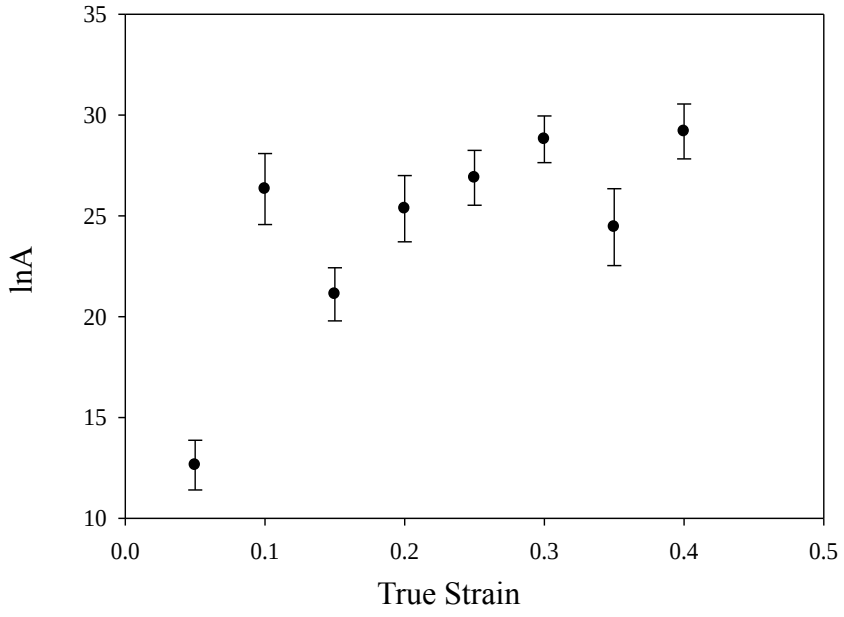

Figure 4.11. Variation of ln*A* with strain for as-cast A535 alloy.

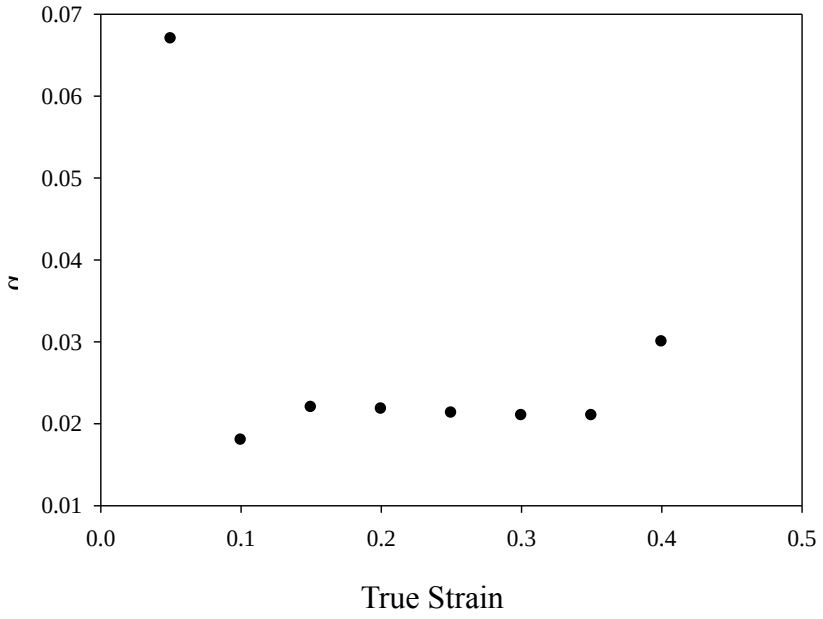

Figure 4.12. Variation of α with strain for as-cast A535 alloy.

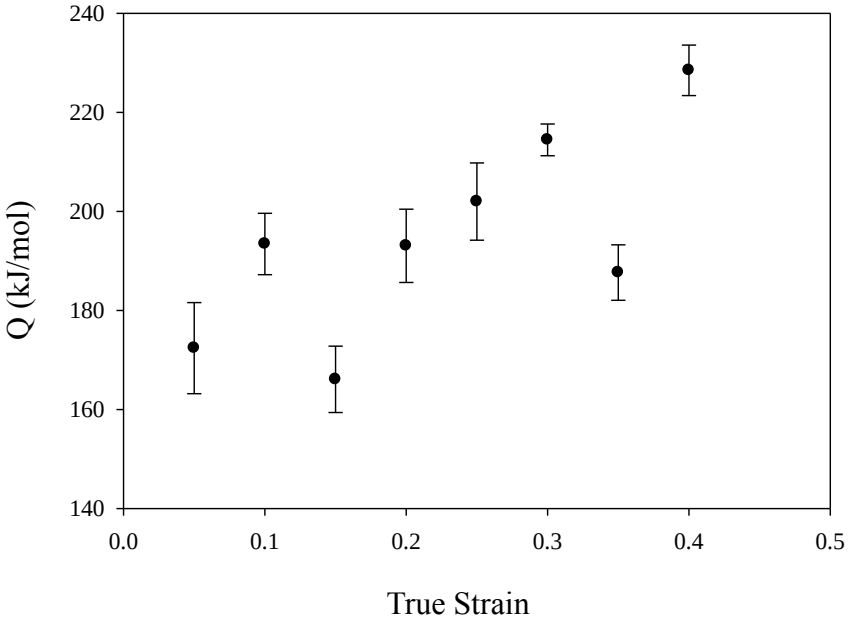

Figure 4.13. Variation of activation energy (*Q*) with strain for as-cast A535 alloy.

As shown in Figure 4.12, α values which were determined by trial and error varied in the range of 0.018 to 0.067 MPa^{-1} with true strain and were assumed as fixed values under all deformation conditions. The value of α was reported to be in the range of 0.01 to 0.08 MPa^{-1} for different Al-Mg alloys [38]. Figures 4.8 to 4.13 showed that all the calculated constants for as-cast and homogenized A535 alloy decreased with strain except for *lnA* and activation energy (*Q*). The activation energy of the alloy varied in the range of 172-228 kJ/mol during the deformation process for both as-cast and homogenized conditions. The increasing trend of the activation energy with true strain (Fig. 4.13) showed that the alloy resisted further deformation, which can be attributed to the effect of the solute atoms on hindering dislocation motions by pinning them in their places. Different trends have been observed for variation of the calculated activation energy with strain for aluminum alloys which used the extended form of constitutive equations due to activation of different deformation mechanisms at elevated temperatures. For instance, an ascending trend of activation energy (*Q*) with strain was reported for AA7075 [17] and AA1070 [90] aluminum alloys, while descending trend was observed for AA7050 [21], AA2124-T851 [45], A356 [91] aluminum alloys. Activation energy (*Q*) is an important parameter in hot forming processes. As such, understanding its fluctuation within deformation could possibly assist manufacturers with saving more energy. For finding the trend of observed material constants versus strain, Sigmaplot^{TM} software was used to find the best fit curves for each material constant. Equation (4.11) shows the model of a polynomial function of order *i*, which attributes variable (*x*) to variable (*y*), where *x* is the independent variable, *y* is the dependent variable, and b_0, b_1,…, b_i are polynomial coefficients. Polynomial order varied from 1 to 7, from which a fifth order was found to show the best correlation (i.e. the highest possible of square of residuals (R^2)) and generalization. Higher order (i.e. >5) polynomial would over-fit thus losing

the ability of true representation and generalization. The obtained fitting equations are shown as a group of functions in the APPENDIX A. The coefficients of fitted equations are shown in the APPENDIX B.

$$y = b_0 \pm b_1 x \pm b_2 x^2 \pm ..... \pm b_i x^i \tag{4.11}$$

After calculating the material constants at different strain values using obtained polynomial functions, it is possible to estimate *Z* values in accordance with equation (4.12), where $l(\varepsilon)$ is the activation energy as a function of strain. *Z* varied with strain due to variation of activation energy throughout the whole deformation operation. The derived flow stress equation (4.8) can be rewritten by substituting of obtained polynomial functions for material constants as indicated in equation (4.13). In this equation, $j(\varepsilon)$ is a function of strain, $l(\varepsilon)$ is activation energy as a function of strain, $k(\varepsilon)$ is *lnA* as a function of strain and $f(\varepsilon)$ is *n* as a function of strain. Substituting all the predicted material constants at each strain helps to predict the flow stress values at selected strains.

$$Z = \dot{\varepsilon} \exp\left(\frac{l(\varepsilon)}{8.314 \times T}\right) \tag{4.12}$$

$$\sigma = \frac{1}{j(\varepsilon)} \ln\left\{\left(\frac{\dot{\varepsilon} \exp\left(\frac{l(\varepsilon)}{8.314 \times T}\right)}{\exp\left(k(\varepsilon)\right)}\right)^{\frac{1}{f(\varepsilon)}} + \left[\left(\frac{\dot{\varepsilon} \exp\left(\frac{l(\varepsilon)}{8.314 \times T}\right)}{\exp\left(k(\varepsilon)\right)}\right)^{\frac{2}{f(\varepsilon)}} + 1\right]^{\frac{1}{2}}\right\} \tag{4.13}$$

Figure 4.14 (the same graph was obtained for homogenized specimens of A535 alloy) compares the calculated flow stress (σ_C) values with the measured flow stress (σ_M) values for as-cast and homogenized A535 alloy for different strain rates and deformation temperatures. Equations (4.14) and (4.15) [92], show the correlation coefficient (*R*) and the average absolute relative error (AARE), respectively. In these equations, (σ_{Mi}) is the i'th measured stress value, (σ_{Ci}) is the i'th calculated stress value, $\bar{\sigma}$ is the mean value of the measured and the calculated stress and *N* is the number of employed stress values in these calculations. These are standard statistical parameters, which measure the predictability of the Arrhenius-type constitutive equations.

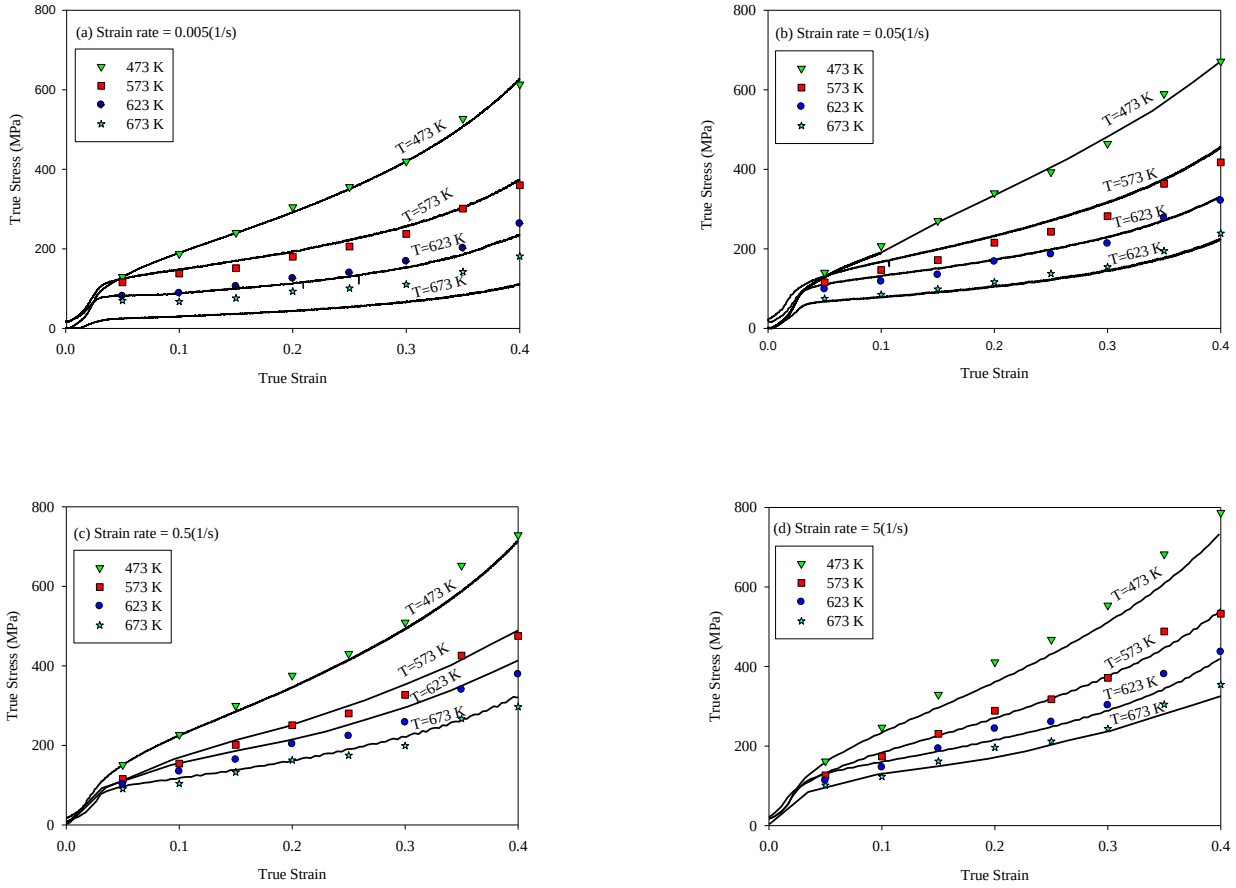

Figure 4.14. Comparison between measured and predicted flow stress curves for as-cast A535 aluminum alloy at different strain rates and different temperatures.

$$R = \frac{\sum_{i=1}^{N}\left(\sigma_{Mi}-\bar{\sigma}\right)\left(\sigma_{Ci}-\bar{\sigma}\right)}{\sqrt{\sum_{i=1}^{N}\left(\sigma_{Mi}-\bar{\sigma}\right)^{2}\sum_{i=1}^{N}\left(\sigma_{Ci}-\bar{\sigma}\right)^{2}}} \tag{4.14}$$

$$AARE\,(\%) = \frac{1}{N}\sum_{i=1}^{N}\left|\frac{\sigma_{Mi}-\sigma_{Ci}}{\sigma_{Mi}}\right| \times 100\% \tag{4.15}$$

The correlation coefficient indicates the strength of linear relationship between the measured and the calculated stress values. The higher correlation coefficient may not necessarily show better predictability of the constitutive equations due to the tendency of the equation to be biased to higher or lower values [92]. The AARE is obtained by calculating the relative error between the

measured and the calculated stress values one-by-one, which makes this statistical equation unbiased for measuring the predictability of the constitutive equations. As shown in Figure 4.14 (a), calculated stress values stand much above the measured flow stress curve for the test condition of T = 673 K and $\dot{\varepsilon}$ = 0.005 s^{-1}. This large difference between the measured and the calculated stress values might be attributed to excessive induced heat transition to the specimen as a result of friction effect during deformation operation. Hence, the computed stress values under this deformation condition were overlooked for calculating correlation coefficient (R) and AARE. All calculated and measured flow stress values with related relative errors are listed in APPENDIX C.

Figure 4.15 (the same graph was obtained for homogenized specimens of A535 alloy) shows that there is a good correlation between the true calculated flow stress values versus the true measured ones by correlation coefficient of R = 0.997. The AARE was calculated to be 6.5%, which shows that the developed constitutive equations provide relatively accurate flow stress curve estimation for as-cast and homogenized A535 aluminum alloy under wide ranges of strain, deformation temperature and strain rate. Quan et al. [17] found sixth order polynomial function as the best fitted curves for variation of all the material constants versus strain for AA7075 aluminum alloy and a maximum relative error of 5.63% between predicted and experimental values was reported. Li et al. [21] used the extended constitutive equations for hot deformation of AA7050 aluminum alloy, by which fifth order polynomial functions were found for all the calculated material constants and a good agreement was found between the calculated and the predicted stress values by average absolute relative error (AARE) of 6.28%. Lin et al. [45] also used a fifth order polynomial function to predict stress values for AA2124-T851 aluminum alloy under hot deformation conditions.

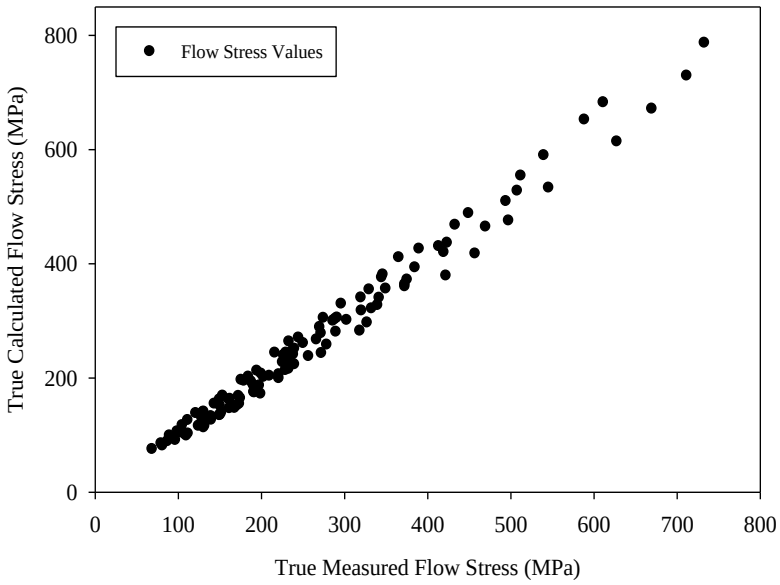

Figure 4.15. Correlation between the measured and the calculated flow stress values for as-cast A535 alloy at different strain rates and deformation temperatures.

The maximum average absolute relative error (AARE) was reported to be 5.91%, which showed good correlation between the measured and the predicted values. Haghdadi et al. [91] employed extended constitutive equations for A356 aluminum alloy and found fifth order polynomial functions of strain for the calculated material constants. Utilizing these functions led to predict flow stress values of the alloy which showed good agreement with the experimental values by absolute average relative error of 8.1%. Rezaei et al. [90] used fifth order polynomial function curves to fit with the material constants of AA1070 aluminum alloy. A good agreement was found between the measured and the predicted stress values of the alloy by a correlation coefficient of 99.2%. However, a wide discrepancy was observed between the measured and the predicted stress values for two deformation conditions (i.e. $\dot{\varepsilon} = 0.5\ s^{-1}$ at $T = 450^{\circ}C$ and $T = 500^{\circ}C$).

4.1.5 Microstructural Evaluation of As-cast and Homogenized A535 Alloy Under Hot Deformation Conditions

Figures 4.16 (a) - (b) show optical micrographs of the polished and etched specimens before compression test for as-cast and homogenized A535 aluminum alloy, respectively. It can be seen that the second phase particles (dark parts) are thicker and larger in as-cast A535 alloy specimens than homogenized specimens. These particles are uniformly distributed through the matrix of both as-cast and homogenized specimens. These clusters of second particles impeded dislocation motion which increased resistance of the alloy against further deformation.

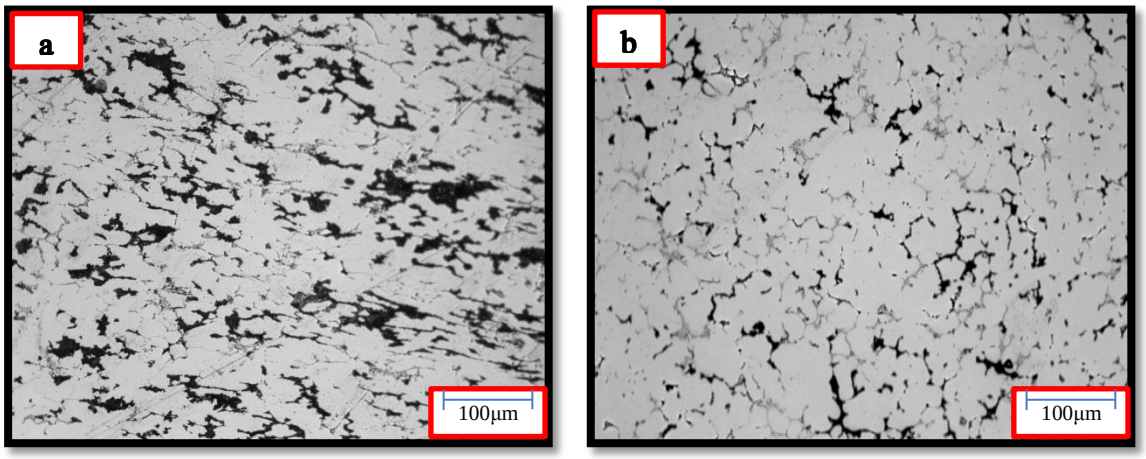

Figure 4.16. Optical micrographs of etched and polished specimens for (a) as-cast A535 and (b) homogenized A535 alloy.

Figures 4.17 (a) - (d) show the optical micrographs for as-cast specimens at different strain rates and temperatures. It is clear that second phase particles were compressed and aligned perpendicular to the applied load direction. Figures 4.18 (a) - (d) show microstructural changes for homogenized A535 specimens under various deformation conditions. Similar microstructural changes were observed for homogenized A535 specimens.

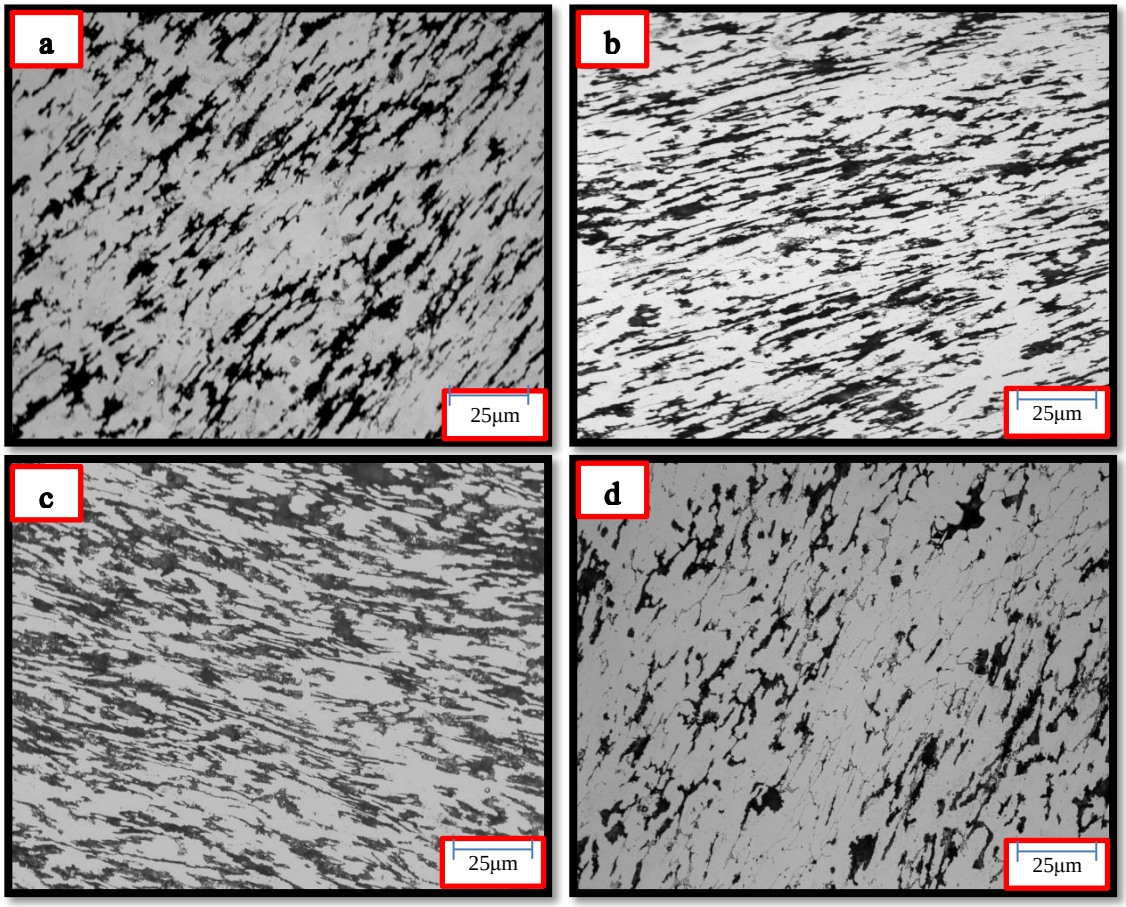

Figure 4.17. Optical micrographs for as-cast A535 alloy under different temperatures and strain rates of (a) T=673 K, $\dot{\varepsilon}$=0.005 s^{-1}, (b) T=623 K, $\dot{\varepsilon}$=0. 05, (c) T=573 K, $\dot{\varepsilon}$=0.5 s^{-1} and (d) T=473, $\dot{\varepsilon}$=5 s^{-1}.

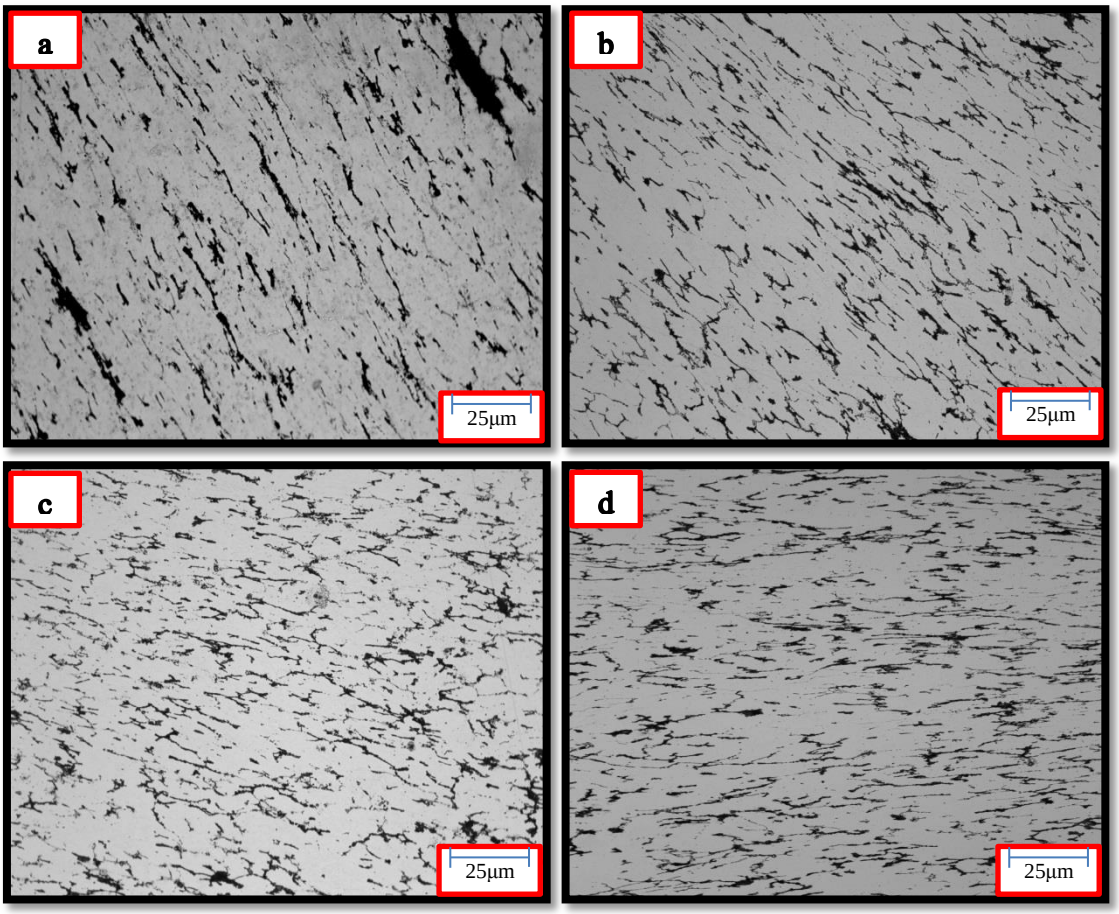

Figure 4.18. Optical micrographs for homogenized A535 alloy under different temperatures and strain rates of (a) T=673 K, $\dot{\varepsilon}$=0.005 s^{-1}, (b) T=623 K, $\dot{\varepsilon}$=0. 05, (c) T=573 K, $\dot{\varepsilon}$=0.5 s^{-1} and (d) T=473, $\dot{\varepsilon}$=5 s^{-1}.

Obtained true stress-true strain curves for as-cast and homogenized A535 alloy (Figures 4.1 and 4.2, respectively) showed that strain hardening mainly controlled the deformation of the alloy at different strain rates and temperatures. By increasing the temperature, mobility of the second phase particles increased which helped them to coalesce and form clusters against applied load.

4.2 High Strain Rate Deformation of A535 Aluminum Alloy

The second part of this research focused on the deformation behavior of the as-cast and homogenized A535 aluminum alloy at high strain rates, which ranged between 1400 and 2400 s^{-1} at room temperature. As previously explained in Chapter 3, the obtained voltage-time data from the oscilloscope were converted to true stress-true strain values, which were analyzed to evaluate the effect of strain rate on the response of the alloy to dynamic impact loading. The microstructure of the as-cast and homogenized A535 specimens were examined after shock loading, using optical microscope and scanning electron microscope to find the effect of various strain rates on the alloy's microstructural evolution.

4.2.1 Quasi-static Compression Test Properties

Figure 4.19 shows obtained flow stress curves under quasi-static and dynamic loading conditions. As can be seen flow stress of the A535 alloy under quasi-static load condition maintained a higher level than the one under dynamic load condition up to the true strain of 0.09. Afterward, the flow stress of the alloy under dynamic load condition increased at a higher rate than under quasi-static load conditions. Under dynamic load condition both strain hardening and thermal softening compete to control the deformation of the impacted material; however, strain hardening is the dominant deformation mechanism under quasi-static load condition. Under dynamic shock loading, about 90% of the kinetic energy of the strike bar converts to heat in the material which activates thermal softening. It is clear that at high strain rates the strain hardening exponent of A535 alloy increased sharply after the yield point until thermal softening began to dominate the deformation process. Zhenxing et al. [93] compared stress strain curves of TiB_2/Al composites under dynamic and static loading, and demonstrated that the material depict higher

levels of stress, and higher levels of elongation under dynamic loading compared to static loading. Similar results were observed for AA2099-T4 alloy [80].

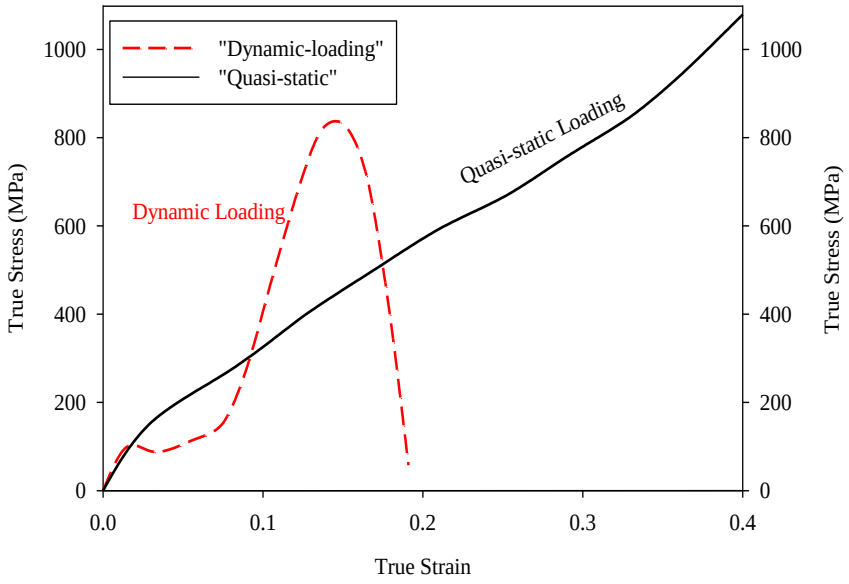

Figure 4.19. Typical true stress-true strain curves for as-cast A535 alloy under dynamic and quasi-static load conditions.

4.2.2 Dynamic Compression Properties

Figure 4.20 (a) - (b) shows the true stress-true strain curves obtained under impact loading at various strain rates for as-cast and homogenized A535 aluminum alloy, respectively. It can be seen that the flow stress of the two sets of specimens varied in a similar pattern with strain at different strain rates, which is an indication that they underwent the same stages of deformation during impact loading. Initially, the alloy deformed elastically up to the first peak, after which the flow stress declined slightly or attained a plateau. Then, as deformation continued, the flow stress increased once again up to the second peak, after which it declined sharply with continued deformation. The gradual decline in flow stress after first peak is believed to be due to low temperature softening activated, during which dislocation movement evolved. The heat for the

thermal softening was produced by conversion of the impact significant energy of the striker to heat in the specimen. The rapid increase in the flow stress following the end of the initial decline is believed to be due to strain hardening produced by rapid multiplication of dislocations accompanying the high impact loading. However, strain hardening did not control the deformation process indefinitely. As deformation continued, the flow stress reached a second maximum and fell drastically due to intense thermal softening. This second softening is believed to be caused by adiabatic heating, which caused intense shear strain localization within the alloy. Intense strain localization in metallic alloys leads to formation of adiabatic shear bands (ASBs) [94].

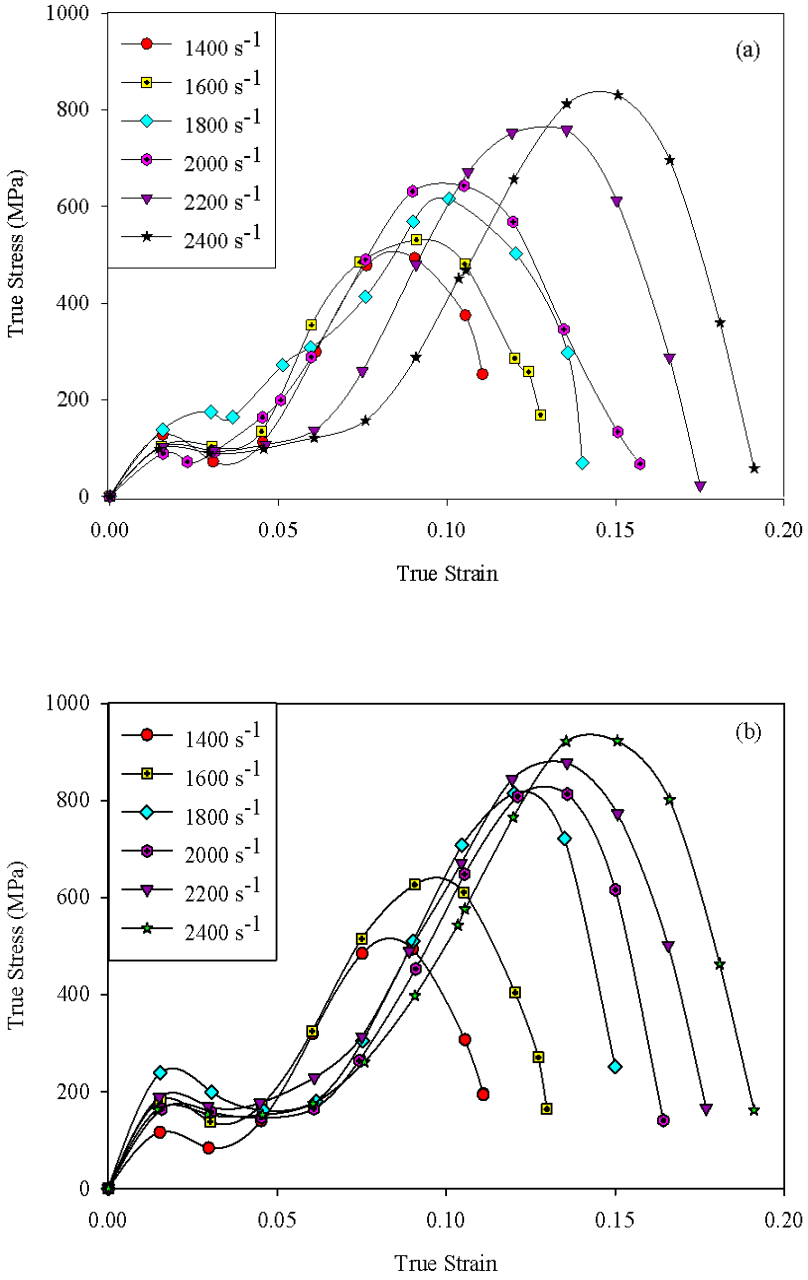

Figure 4.20. Typical true stress-true strain curves obtained for specimens of A535 aluminum alloy at different strain rates: (a) as-cast (b) homogenized.

4.2.2.1 Effect of Homogenization Heat Treatment

Although the overall trend of flow stress versus strain curves is similar for both as-cast and homogenized specimens of A535 alloy, as shown in Figure 4.20, a close look points to some salient differences. To help bring out these differences, the stress-strain curves obtained for each strain rate are co-plotted in Figures 4.21 (a) - (f) for as-cast and homogenized specimens. One main difference is that the peak flow stresses of homogenized A535 (i.e. the first and second peak stresses) are higher than those of the as-cast counterpart. The area under the stress-strain curves for homogenized specimens is larger than that for the as-cast specimens. Therefore, the toughness of homogenized specimens is higher compared to the toughness of as-cast specimens. The higher peak stresses obtained for the homogenized specimens indicates that they resisted thermal softening more than as-cast specimens. Odeshi et al. [52] reported that the mechanical response of AISI 4340 steel to dynamic shock loading was substantially affected by the type of heat treatment and strain rate. They found that the starting time and the strain at which their samples experienced thermal softening was increased for specimens tempered at lower temperatures. However, the obtained stress-strain curves indicated that the higher the strain rate the sooner the onset of thermal softening, which is in contrast with the results obtained for as-cast and homogenized A535 aluminum alloy. Odeshi et al. [80] investigated the effect of different tempers (e.g.,T4, T6 and T8) on the mechanical response of AA6061 and AA2099 aluminum alloys under high strain rates. AA2099 showed the highest tendency to adiabatic shear strain failure in the T8 temper while AA6061 was more prone to strain localization failure in the T4 temper. From this it can be deduced that thermal softening resistance for the AA2099 alloy reached the optimum point after T4 heat treatment, while T8 heat treatment ameliorated AA6061 mechanical response under impact loading. Additionally, the pattern of crack propagation was

found to be different in the two alloys. While failure crack initiated and grew along the interface of shear band and bulk material in AA2099 alloy, it was propagated through the central line of white shear bands in AA6061 alloy. The effect of different heat treatments on Al-Li alloy [66] mechanical response under shock loading condition revealed that deformed and transformed shear bands were formed under all circumstances. However, the width and the length of the shear band varied under various thermal treatments and temperatures. It was reported that the propensity for crack initiation and propagation was higher at lower temperatures than of the ambient temperature.

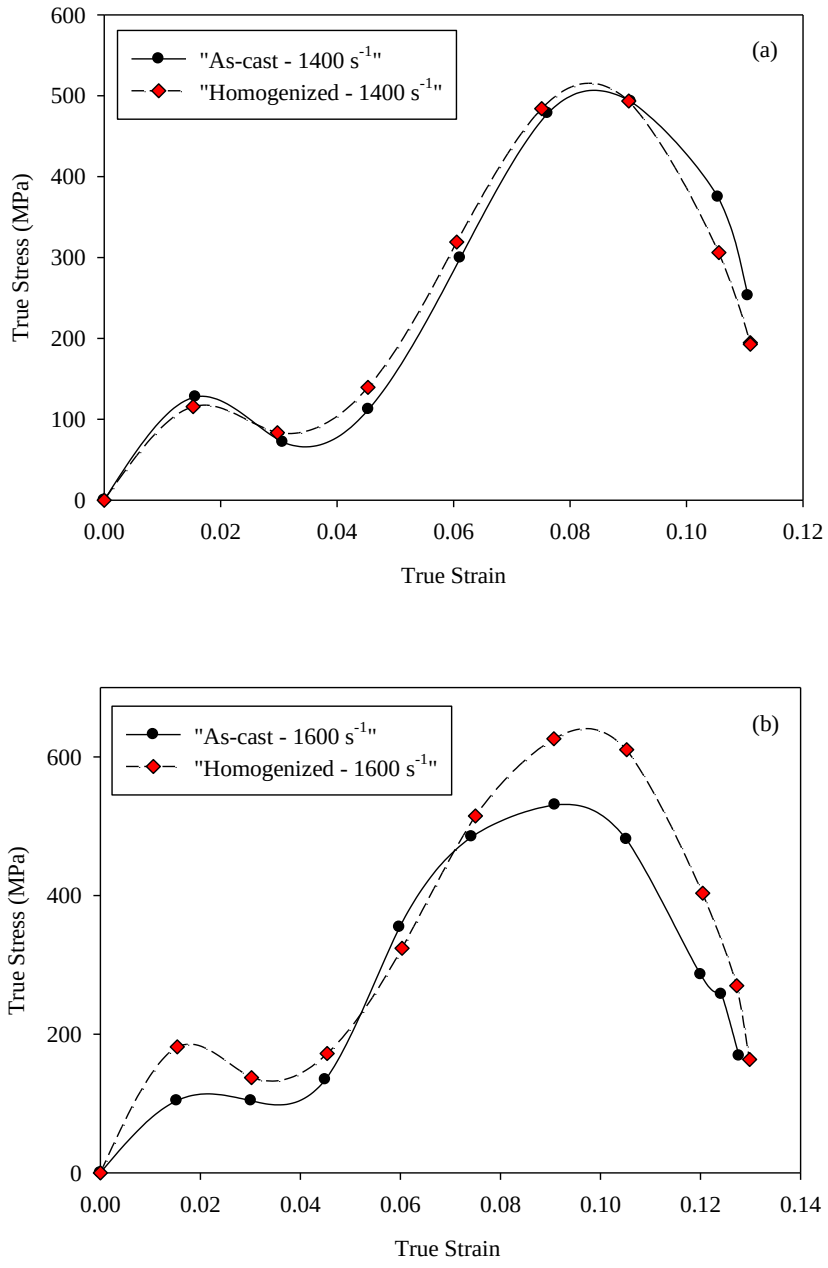

Figure 4.21. Comparison of true stress-true strain curves obtained for as-cast and homogenized A535 aluminum alloy of different strain rates: (a) 1400 s^{-1}, (b) 1600 s^{-1}, (c) 1800 s^{-1}, (d) 2000 s^{-1}, (e) 2200 s^{-1} and (f) 2400 s^{-1}.

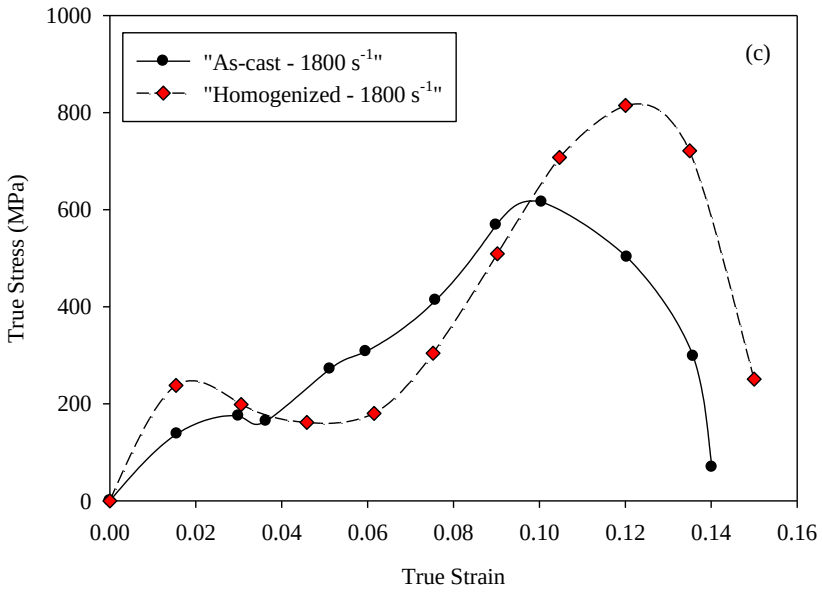

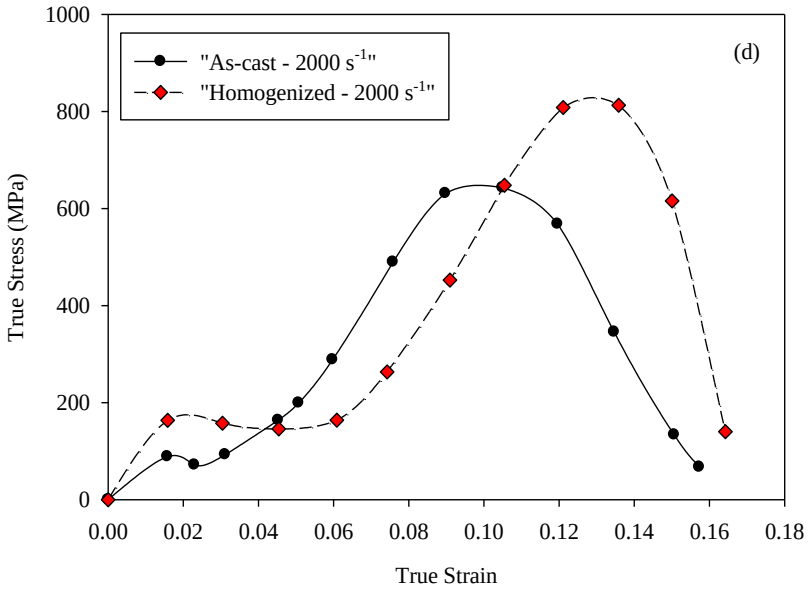

Figure 4.21. Continued.

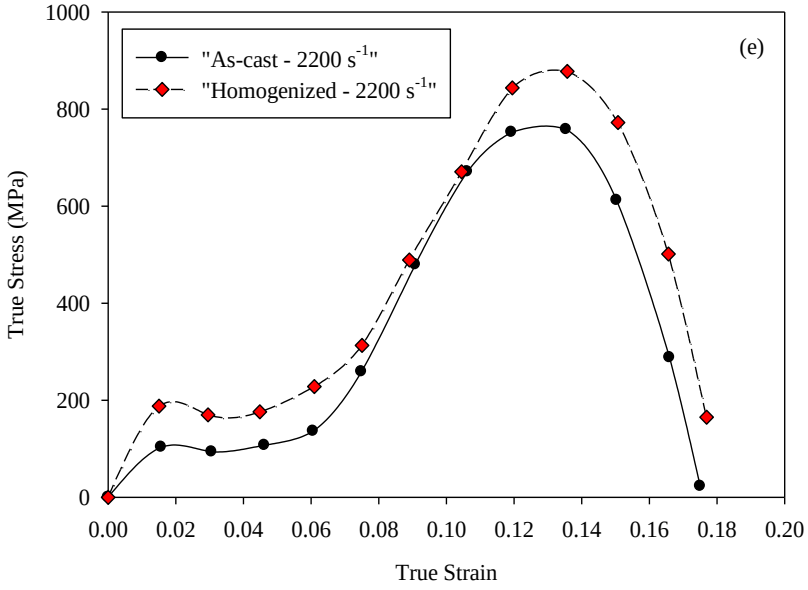

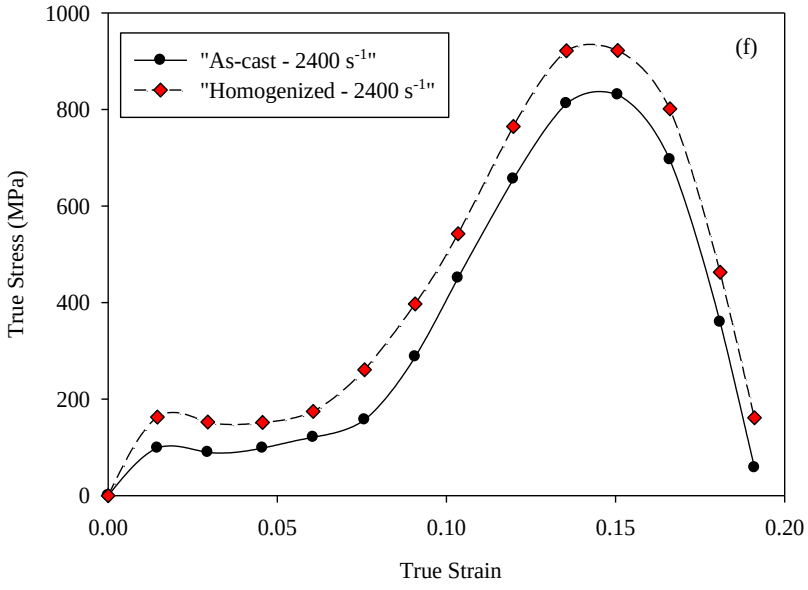

Figure 4.21. Continued.

4.2.2.2 Effect of Strain Rate

A close examination of the true stress-true strain curves of the Figure 4.20 reveals that the second peak of the flow stress shifted to the right as strain rate increased. The area under the stress-strain curves increased with increasing strain rate, which indicates that impact energy absorption of A535 alloy increased with increasing strain rate. Also, it can be seen that the strain at which thermal softening started to dominate strain hardening very strongly (the so-called critical strain) increased with increasing strain rate. This implies that raising strain rate delays the onset of adiabatic shear localization in the A535 alloy. Adesola et al. [95] observed that the peak stress of AA6061 showed ascending trend with increasing impact loading from 33 to 39 kg m/s for all temper conditions (i.e. T4, T6 and T8). However, the peak stress of the alloy for T4 and T6 decreased by increasing impact loading from 39 to 44 kg m/s. It shows that AA6061 alloy showed higher thermal softening resistance under impact loading for T8 temper condition than those for T4 and T6 conditions.

It is clear from the preceding observations that A535 alloy is sensitive to the strain rate at room temperature. To determine the influence of homogenization heat treatment and strain rate on the peak stress of the alloy, the strain rate sensitivity (m) of peak stress for each set of specimens were calculated and compared. By definition,

$$\sigma = C\dot{\varepsilon}^{m} \tag{4.16}$$

where σ = stress (MPa), C = is a constant (MPa s) and $\dot{\varepsilon}$ = strain rate (s^{-1}). Taking logarithm on both sides yields:

$$\ln\sigma = \ln C + m\ln\dot{\varepsilon} \tag{4.17}$$

For each sets of specimens, m was calculated from the slope of lnσ versus lnε̇ graphs using a linear regression method. The stress used was the peak stress (the second peak of Figure 4.20)

and the strain rate used was that corresponding to the peak stress. The strain rate sensitivities for as-cast and homogenized A535 specimens were calculated to be 0.97 and 1.13, respectively. Figure 4.22 shows the variation of strain rate sensitivity with strain rate for as-cast and homogenized A535 alloy. It is clear that the strain rate sensitivity of peak stress values for homogenized A535 alloy is slightly higher than that of as-cast alloy and for both conditions the alloy shows positive strain rate sensitivity. Oosterkamp et al. [96] found a slight increase of strain rate sensitivity for AA6082 and AA7108 aluminum alloys at strain rates lower than 2000 s^{-1}. However, the trend of strain rate sensitivity was changed at strain rates higher than 2000 s^{-1}, due to softening effect of shear strain localization. Positive strain rate sensitivity was reported for Al-Sc alloy under dynamic load conditions [49].

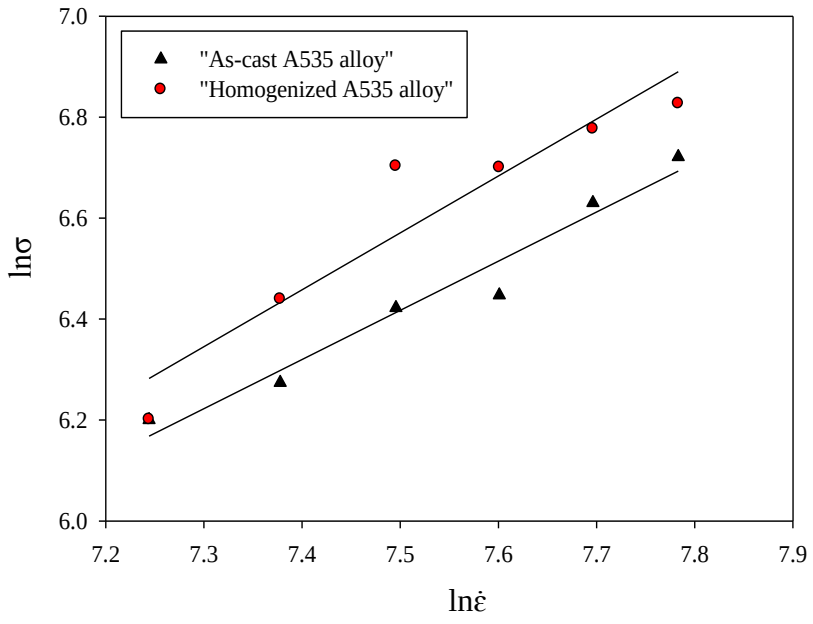

Fig 4.22. Variation of strain rate sensitivity for the peak stress values of as-cast and homogenized A535 aluminum alloy with strain rate.

4.2.3 Microstructural Evaluation

Microstructural examination of tested specimens of A535 aluminum alloys at various strain rates showed that adiabatic shear bands (ASBs) formed at strain rates above 2000 s^{-1} in both as-cast and homogenized conditions. Figures 4.23 (a) - (b) show the zones of DSBs of polished and etched specimens for as-cast and homogenized A535 alloys, respectively, which formed at a strain rate of 2200 s^{-1}. Figures 4.24 and 4.25 show the obtained microstructures of inside adiabatic shear bands (ASBs) formed at different strain rates for as-cast and homogenized A535 specimens, respectively. As shown in these micrographs, the width of the second particles (dark areas) were decreased by increasing the strain rate from 2200 s^{-1} to 2400 s^{-1} for both as-cast and homogenized A535 specimens. The second particles were aligned and elongated in the direction of stress wave propagation through the matrix. Since FCC metals such as aluminum alloys are known as high stacking fault energy metals, they are less susceptible to form transformed shear bands (TSBs) [70, 71]. Microstructural examination of a cold rolled high purity aluminum which was compressed under high strain rate loading showed that there was no adiabatic shear band formation unless the degree of deformation approached 90% [72]. Although deformed shear bands (DSBs) and transformed shear bands (TSBs) were observed in several aluminum alloys under dynamic loading [39, 97-99], A535 aluminum alloy showed only deformed shear bands (DSB) under dynamic shock load condition for the range of strain rate investigated.

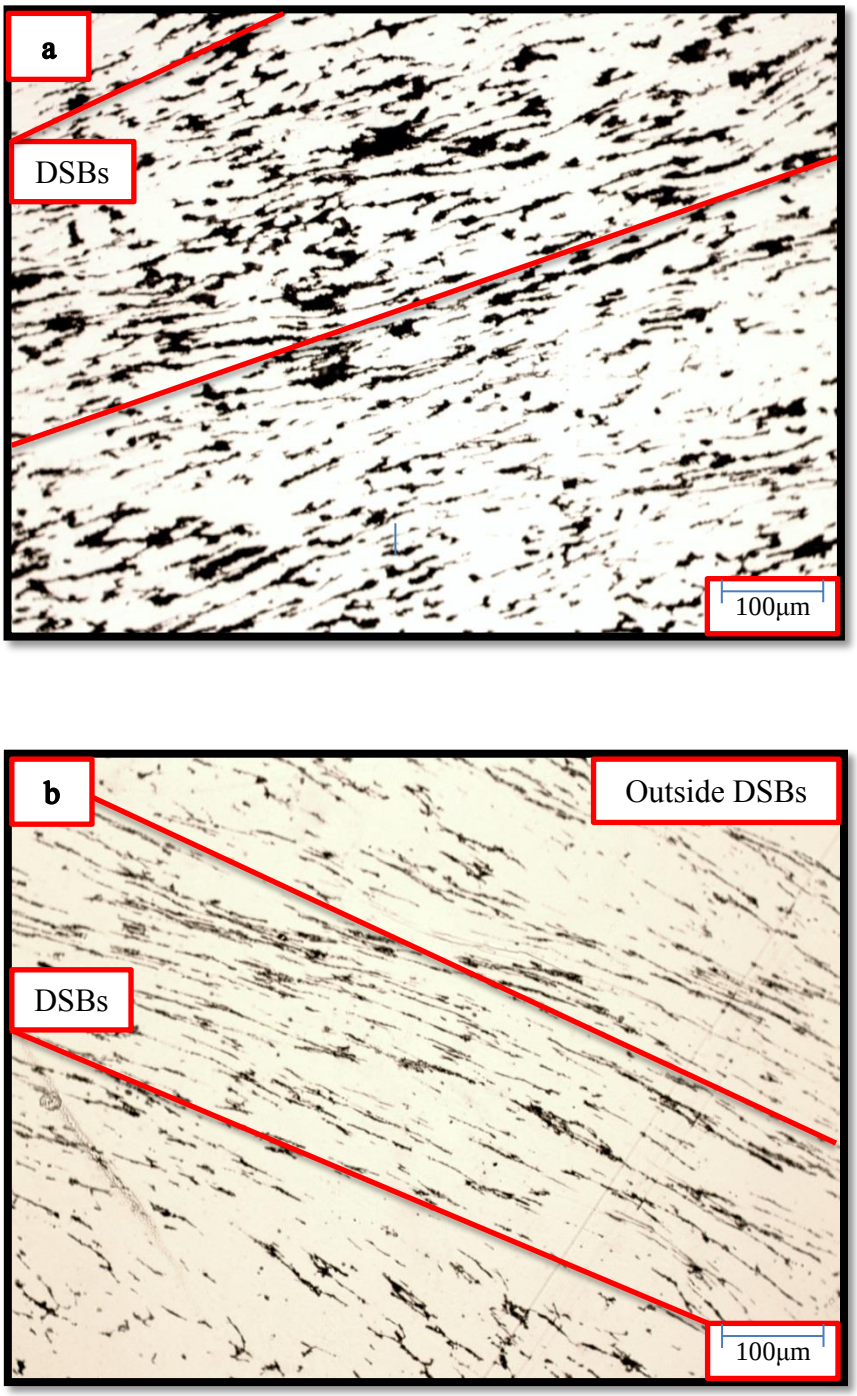

Figure 4.23. Optical micrographs of deformed shear bands formation (DSBs) for (a) as-cast A535 alloy (b) homogenized A535 alloy at the strain rate of 2200 s^{-1}.

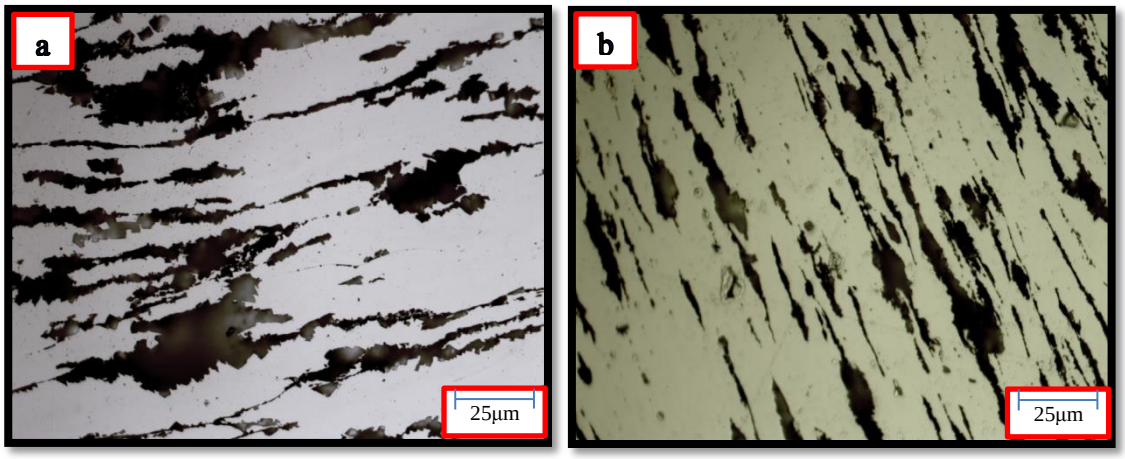

Figure 4.24. Optical micrograph showing morphology of inside deformed shear bands (DSBs) for as-cast A535 alloy at strain rates of (a) 2200 s^{-1} (b) 2400 s^{-1}.

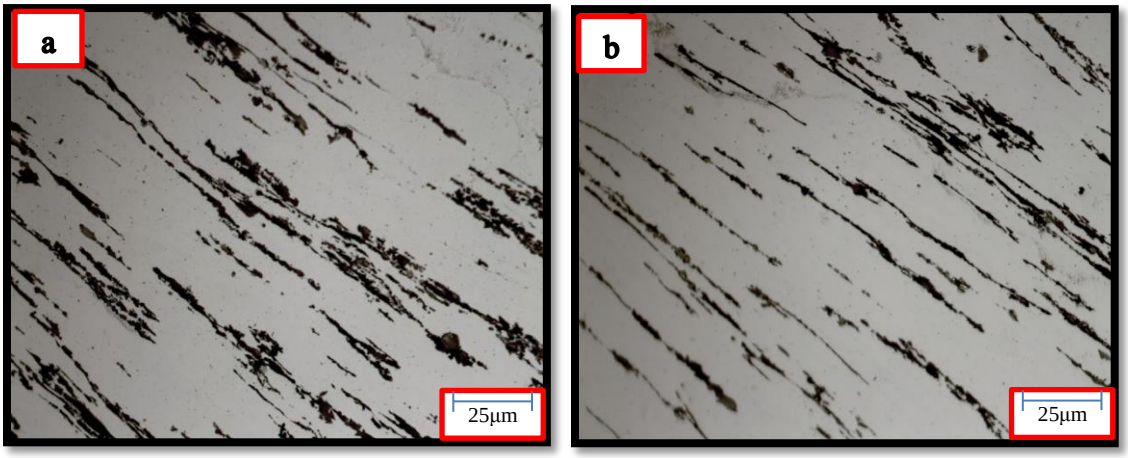

Figure 4.25. Optical micrograph showing morphology of inside deformed shear bands (DSBs) for homogenized A535 alloy at strain rates of (a) 2200 s^{-1} (b) 2400 s^{-1}.

Figure 4.26 shows the morphology and distribution of the second phase particles outside the ASB zone at a strain rate of 2200 s^{-1}, in which the second particles are less compacted and deformed, compared to those inside the ASB zone. Figures 4.27 and 4.28 show SEM images of microstructural changes inside ASBs formed for as-cast and homogenized A535 specimens at strain rates of 2200 s^{-1} and 2400 s^{-1}, respectively. It can be seen that the volume fraction and size

of second phase particles in the matrix of as-cast specimens are higher than homogenized ones. Obtained true stress-true strain curves for A535 alloy showed that the peak stress and the onset thermal softening strain were higher for homogenized specimens than as-cast specimens. It has been found that second phase particles play an important role in initiating adiabatic shear bands (ASBs) formation in metals [100, 101]. Therefore, the higher onset thermal softening strain in homogenized A535 specimens can be attributed to the lower volume of second phase particles in its matrix than as-cast specimens. Odeshi et al. [79] examined the obtained microstructures of AA5083-H131 and AA606-T6 aluminum alloys under dynamic loading. They reported DSBs formation for AA5083 alloy and TSBs formation for AA6061 alloy. The propensity for forming TSBs in AA6061 alloy was higher than AA5083 alloy due to existence of more second phase particles in its matrix. Xu et al. [66] also reported TSBs formation for Al-Li alloy under high strain rates.

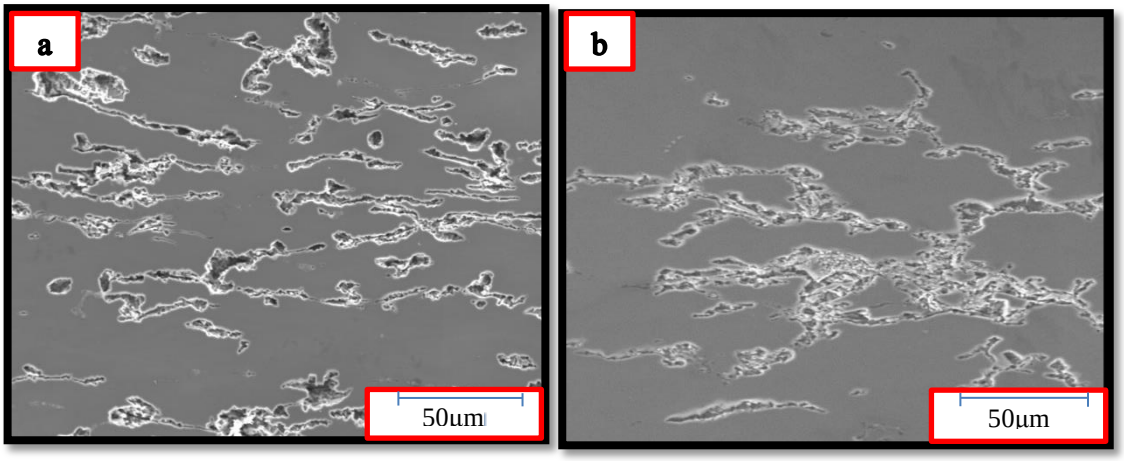

Figure 4.26. SEM micrographs showing the morphology and distribution of the second phase particles outside of the ASBs' zone for (a) as-cast and (b) homogenized A535 alloy at the strain rate of 2200 s^{-1}.

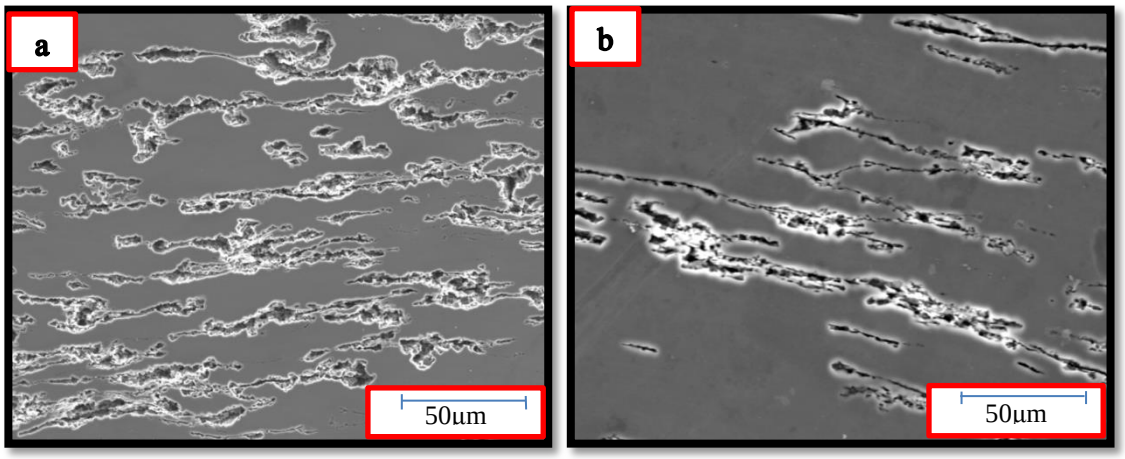

Figure 4.27. SEM micrographs showing the morphology and distribution of the second phase particles inside the DSBs for (a) as-cast and (b) homogenized A535 alloy at the strain rates of 2200 s^{-1}.

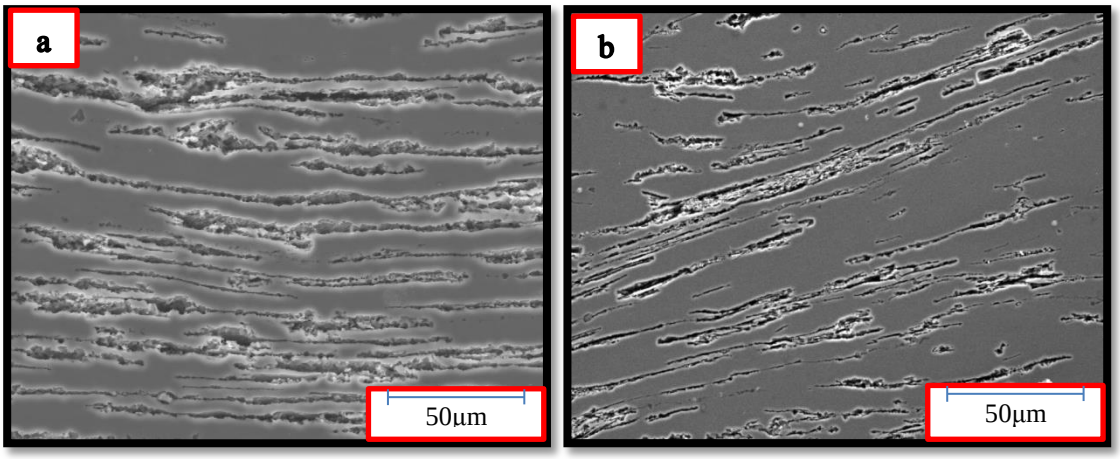

Figure 4.28. SEM micrographs showing the morphology and distribution of the second phase particles inside the DSBs for (a) as-cast and (b) homogenized A535 alloy at the strain rates of 2400 s^{-1}.

CHAPTER 5

CONCLUSIONS AND RECOMMENDATIONS

This research focused on two main topics. In the first one, the flow stress behavior of A535 aluminum alloys in as-cast and homogenized conditions was investigated at elevated temperatures and low strain rates using a Gleeble^{TM} simulation machine. In the second, the mechanical response of as-cast and homogenized A535 alloy to high dynamic shock loading was investigated at room temperature using a SHPB machine. The material and experimental methods used in these investigations were presented in Chapter 3, while the obtained results were presented and discussed in Chapter 4. The present chapter presents the conclusions derived from analyzing the results and provides suggestions for future work.

5.1 Hot Deformation Behavior of A535 Aluminum Alloy

1. The flow stress of A535 alloy increased with increasing strain rate and decreasing deformation temperature. Obtained true stress-true strain curves for as-cast and homogenized conditions were compared and no difference was found between them under elevated temperatures quasi-static load tests.
2. Fitting obtained experimental data to Arrhenius-type constitutive equations yielded material constants such as n, n', β, A and activation energy (Q), which is an important physical parameter for hot deformation processes of metals. Activation energy (Q) was calculated to be 193 kJ/mol for as-cast and homogenized A535 alloys, which is higher than that for the self-diffusion of pure aluminum (142 kJ/mol).

3. Strain rate sensitivity was calculated to be the same for both as-cast and homogenized A535 alloys and increased by increasing deformation temperature.
4. To evaluate the effect of strain on the material constants, Arrhenius-type constitutive equations were extended through various strain points. It was found that all the calculated constants of as-cast and homogenized A535 alloy varied with strain. The activation energy of A535 alloy increased by increasing strain for both as-cast and homogenized conditions. Additionally, polynomial curves of fifth order were fitted to define the variation of all calculated material constants with strain.
5. Flow stress values at different strains were calculated using the extended form of Arrhenius-type constitutive equations under different strain rates and temperatures. The calculated flow stress values showed good agreement with the measured values for both as-cast and homogenized A535 alloys, by the correlation coefficient of 0.997 and the average absolute relative error (AARE) of 6.5%.

5.2 High Strain Rate Deformation Behavior of A535 Aluminum Alloy

1. The peak stress and critical strain at the onset of thermal softening increased with strain rate for both as-cast and homogenized specimens of A535 alloy.
2. Homogenization heat treatment affected the high strain rate deformation of A535 alloy. The peak stress at the onset of thermal softening increased after heat treatment.
3. Strain rate sensitivity of the peak stress values for A535 aluminum alloy was increased after homogenization heat treatment.
4. Deformed shear bands (DSBs) were formed at strain rates higher than 2000 s^{-1} for both as-cast and homogenized A535 alloy.

5.3 Suggestions for Future Work

1. Examine microstructural changes of the A535 aluminum alloy under hot deformation conditions using transmission electron microscopy (TEM) to study dislocation behavior at different strain rates and temperatures.
2. Conduct high strain rate deformation test at elevated temperatures to investigate the effect of temperature on the mechanical behavior of the A535 alloy under shock loading condition and compare it with the results obtained for quasi-static tests at elevated temperatures.

EFERENCES

1. W.S. Miller, L. Zhuang, J. Bottema, A.J. Wittebrood, P. De Smet, A. Haszler and A. Vieregge, "Recent development in aluminium alloys for the automobile industry", Materials Science and Engineering Failure Analysis A, vol. 280, pp. 37–49, 2000.

2. T. Sakurai, "The latest trends in aluminum alloy sheets for automobile body panels", Kobelco Technology Review , Vol. 28, 2008.

3. T.S. Turrentine and K.S. Kenneth, "Car buyers and fuel economy?", Energy Policy , Vol. 35, pp. 1213-1223, 2007.

4. D. Austin and T. Dinan, "Clearing the air: the costs and consequences of higher CAFE standards and increased gasoline taxes", Environmental Economics and Management, vol. 50,pp. 562-582, 2005.

5. EPA's Office of Transportation and Air Quality, "EPA and NHTSA set standards to reduce greenhouse gases and improve fuel economy for model years 2017-2025 cars and light trucks", http://www.epa.gov, [Accessed on Oct, 2013].

6. G.S. Cole and A.M. Sherman, "Light weight materials for automotive applications", Materials Characterization, vol. 35, pp. 3-9, 1995.

7. S. Das, "The life-cycle impacts of aluminum body-in-white automotive material", Journal of Minerals, Metals and Materials Society (JOM), vol. 52, pp. 41-44, 2000.

8. L. Cheah, J. Heywood and R. Kirchain, "Aluminum stock and flows in US passenger vehicles and implications for energy use", Journal of Industrial Ecology, vol. 13, pp. 718-734, 2009.

9. Ducker Worldwide, "Aluminum Association Auto and Light Truck Group 2009 Update on Aluminum Content in North American Light Vehicles", Troy, Michigan, Phase I, 2008.

10. J. R. Davis, "ASM specialty handbook: aluminum and aluminum alloys", ASM International, Materilas Park Ohio, pp. 784, 1993.

11. Aluminum Association, "Aluminum: properties and physical metallurgy", Edited by J.E. Hatch, ASM International, Materilas Park Ohio, pp. 424, 1984.

12. P.C. Varley, "The technology of aluminium and its alloys", Newnes-Butterworths, Cleveland, Ohio, pp. 161, 1970.

13. R.E. Reed-Hill and R. Abbaschian, "Physical metallurgy principles", Van Nostrand, Michigan, pp. 920, 1973.

14. J.R. Davis, "Properties and selection: nonferrous alloys and special-purpose materials", ASM Internationals, Materilas Park Ohio, vol. 2, pp. 1328, 1990.

15. R.D. Dohertya, D.A. Hughesb, F.J. Humphreysc, J.J. Jonasd, D.Juul Jensene, M.E. Kassnerf, W.E. Kingg, T.R. McNelleyh, H.J. McQueeni and A.D. Rollettj, "Current issues in recrystallization: A review", Material Science and Engineering A, vol. 238, pp. 219-274, 1997.

16. A. Laasraoui and J.J. Jonas, "Prediction of steel flow stresses at high temperatures and strain rates", Metallurgical Transactions A, vol. 22, pp. 1545-1558, 1991.

17. G.Z. Quan, G.S. Li, Y. Wang, W.Q. Lv, C.T. Yu and J. Zhou "A characterization for the flow behavior of as-extruded 7075 aluminum alloy by the improved Arrhenius model with variable parameters", Materials Research, vol. 16, pp. 19-27, 2013.

18. N. Jin, H.Zhang, Y. Han, W. Wu and J. Chen, "Hot deformation behavior of 7150 aluminum alloy during compression at elevated temperature", Materials Characterization, vol. 60, pp. 530-536, 2009.

19. C. Shi, W. Mao and X. Chen, "Evolution of activation energy during hot deformation of AA7150 aluminum alloy", Materials Science and Engineering A, vol. 571, pp. 83-9, 2013.

20. Y. Deng, Z. Yin, and J. Huang, "Hot deformation behavior and microstructural evolution of homogenized 7050 aluminum alloy during compression at elevated temperature", Materials Science and Engineering A, vol. 528, pp. 1780-1786, 2011.

21. J. Li, J. Cai, R. Wang, Z. Yuan and F. Xue, "Flow behavior modeling of the 7050 aluminum alloy at elevated temperatures considering the compensation of strain", Materials & Design, vol. 42, pp. 369-377, 2012.

22. X. W. Yang, Z. H. Lai, J. C. Zhu, Y. Liu and D. He, , "Hot compressive deformation behavior Of the as-quenched A357 aluminum alloy", Materials Science and Engineering B, vol. 177, pp. 1721-1725, 2012.

23. C. M. Estey, S. L. Cockcroft, D. M. Maijer and C. Hermesmann, "Constitutive behaviour of A356 during the quenching operation", Materials Science and Engineering A, vol. 383, pp. 245-251, 2004.

24. R. Carmona, Q. Zhu, C. M. Sellars and J. H. Beynon, , "Controlling mechanisms of deformation of AA5052 aluminium alloy at small strains under hot working condition", Materials Science and Engineering A, vol. 393, pp. 157-163, 2005.

25. S.R. Chen, M.G. Stout, U.F. Kocks, S.R. MacEwen, A.J. Beaudoin, "Constitutive modeling of a 5182 aluminum as a function of strain rate and tempeature", Hot Deformation Of Aluminum Alloys II Symposium, 1998.

26. G. R. Ebrahimi, A. Zarei-Hanzaki, M. Haghshenas and H. Arabshahi, “The effect of heat treatment on hot deformation behaviour of Al 2024”, Materials Processing Technology, vol. 206, pp. 25-29, 2008.

27. S. Chen, K. Chen, G. Peng, X. Chen and Q. Ceng, “Effect of heat treatment on hot deformation behavior and microstructure evolution of 7085 aluminum alloy”, Alloys and Compounds, vol. 537, pp. 338-345, 2012.

28. B. Zhang and T.N Baker, “Effect of heat treatment on the hot deformation behaviour of AA6082 alloy”, Materials Processing Technology, vol. 153, pp. 881-885, 200429.

29. H. J. McQueen, X. Xia, Y. Cui, B. Li and Q. Meng, “Solution and precipitation effects on hot workability of 6201 alloy”, Materials and Science Engineering A, vol. 319, pp. 420-424, 2001.

30. J. Zhang, B. Chen and Z. Baoxiang, “Effect of initial microstructure on the hot compression deformation behavior of a 2219 aluminum alloy”, Materials and Design, vol. 34, pp. 15-21, 2012.

31. G. Meng, B. Li, H. Li, H. Huang and Z. Nie, “Hot deformation and processing maps of an Al–5.7wt.%Mg alloy with erbium”, Materials Science and Engineering A, vol. 517, pp. 132-137, 2009.

32. H.Z. Li, X.M. Zhang, M. Chen and Z.P. Zhou, “Effects of Ag on microstructure and mechanical properties of 2519 aluminum alloy”, Journal of Central South University of Technology, vol. 13, pp. 130-134, 2006.

33. H. Zhang, L. Li, D. Yuan and D. Peng, “Hot deformation behavior of the new Al-Mg-Si-Cu aluminum alloy during compression at elevated temperatures”, Materials Characterization, vol. 58, pp. 168-173, 2007.

34. J. Luo, M. Q. Li, D and W. Ma, “The deformation behavior and processing maps in the isothermal compression of 7A09 aluminum alloy”, Materials Science and Engineering A, vol. 532, pp. 548-557, 2012.

35. R. Liang and S. Khan Akhtar, “A critical review of experimental results and constitutive models for BCC and FCC metals over a wide range of strain rates and temperatures”, International Journal of Plasticity, vol. 15, pp. 963-980, 1999.

36. H. Shin, J. B. Kim, “A phenomenological constitutive equation to describe various flow stress behaviors of materials in wide strain rate and temperature regimes”, Journal of Engineering Materials and Technology, vol. 132, pp. 0210091-6, 2010.

37. A. Rusinek, J. A. Rodríguez-Martínez and A. Arias, “A thermo-viscoplastic constitutive model for FCC metals with application to OFHC copper”, International Journal of Mechanical Sciences, vol. 52, pp. 120-135, 2010.

38. H.J. McQueen and N. Rayan, “Constitutive analysis in hot working”, Materials Science and Engineering A, Vol. 322, pp. 43-63, 2002.

39. C. Zener and J.H. Hollomon, “Effect of strain-rate upon the plastic flow of steel”, Applied Physics, vol. 15, pp. 22-7, 1944.

40. C.M. Sellars and W.J. McTegart, “On the mechanism of hot deformation”, Acta Metallurgica, vol. 14, pp. 1136-8, 1966.

41. O. D. Sherby, H. K. Rodney and A. K.Miller, “Flow stress, subgrain size, and subgrain stability at elevated temperature”, Metallurgical Transactions A, vol. 8, pp. 843-850, 197742.

42. M. R. Rokni, A. Zarei-Hanzaki, A. Roostaei and A. Abolhasani, “Constitutive base analysis of a 7075 aluminum alloy during hot compression testing”, Materials and Design, vol. 32, pp. 4955-4960, 2011.

43. Y.C. Lin, Q.F. Li, Y.C. Xia and L.T. Li, “A phenomenological constitutive model for high temperature flow stress prediction of Al-Cu-Mg alloy”, Materials Science and Engineering A, vol. 534, pp. 654-662, 2012.

44. Z.S. Guo Junhang, R. Murakami, R. Ding and S. Fan, “Modeling the hot deformation behavior of Al alloy 3003”, Journal of Alloys and Compounds, vol. 566, pp. 62-67, 2013.

45. Y.C. Lin, Y.C. Xia, X.C. Chen and M.S. Chen, “Constitutive descriptions for hot compressed 2124-T851 aluminum alloy over a wide range of temperature and strain rate”, Computational Materials Science, vol. 50, pp. 227-233, 2010.

46. Y. Chen, A.H Clausen, O. S Hopperstad and M. Langseth, “Stress–strain behavior of aluminium alloys at a wide range of strain rates”, International Journal of Solids and Structures, vol. 46, pp. 3825-3835, 2009.

47. J. E Field, S. M Walley, W. G Proud, H. T Goldrein and C. R Siviour, “Review of experimental techniques for high rate deformation and shock studies”, International Journal of Impact Engineering, vol. 30, pp. 725-775, 2004.

48. C. Albertini, M. Montagnani, “Wave propagation effects in dynamic loading”, Nuclear Engineering and Design, vol. 37, pp. 115-124, 1976.

49. W. S. Lee, T. H. Chen, C. F Lin and G. T. Lu, “Adiabatic shearing localisation in high strain rate deformation of Al-Sc Alloy”, Materials Transactions, vol. 51, pp. 1216-1221, 2010.

50. S.C. Liao and J. Duffy, “Adiabatic shear bands in a Ti-6Al-4V titanium Alloy”, Journal of the Mechanics and Physics of Solids, vol. 46, pp. 2201-2231, 1998.

51. M. G. da Silva and K. T. Ramesh, “The rate-dependent deformation and localization of fully dense and porous Ti-6Al-4V”, Matererials Science Engineering A, vol. 232, pp. 11-22, 1997.

52. A.G. Odeshi, S. Al-ameeri and M.N. Bassim, “Effect of high strain rate on plastic deformation of a low alloy steel subjected to ballistic impact”, Materials Processing Technology, vo. 162-163, pp. 385-391, 2005.

53. S.P. Timothy and I.M. Hutchings, “Structure of adiabatic shear bands In metals: a critical review”, Acta Metallurgica, vol. 35, pp. 301-306, 1987.

54. R.J. Clifton, “Material response to ultra-high loading rates”, Report NMAB-356, National Advisory Board Committee, 1980.

55. M.A. Meyers and E.M. Lawrence, “Shock-waves and high-strain-rate phenomena in metals”, Plenum Press, New York, pp. 277, 1981.

56. A. Molinari and R.J. Clifton, “Viscoplastic strain localization in simple shear mode: exact results in non-linear theory”, CRAS Series II, vol. 296, pp. 1-4, 1983.

57. D.E. Grady and M.E. Kipp, “The growth of unstable thermoplastic shear with application to steady-wave shock compression in solids”, Journal of the Mechanics and Physics of Solids, vol. 35, pp. 95-119, 1987.

58. L.S. Costin, E.E. Crisman, R. H. Hawley, and J. Duffy, "On the localisation of plastic flow in mild steel tubes under dynamic torsional loading", In Proc. 2 nd Conference, Mechanical Properties of Materials at High Rates of Strain, Oxford, England, pp. 90-100. 1980.

59. K.A, Hartley, J. Duffy and R.H. Hawley, “Measurement of the temperature profile during shear band formation in steels deforming at high strain rates”, Journal of the Mechanics and Physics of Solids, vol. 35, pp. 283-301, 1987.

60. A. Marchand, J. Duffy J, “An experimental study of the formation process of adiabatic shear bands in a structural steel”, Journal of the Mechanics and Physics of Solids, Vol. 36, pp. 251-283, 1988.

61. R.W.Rohde, B.M. Butcher J.R. Holland and C.H. Karens, “Metallurgical effects at high strain rates”, Plenum Press, Newyork-London, pp. 684, 1973.

62. M.A. Meyers and L.E. Murr, “Shock waves and high-strain-rate phenomena in metals”, In Proceeding, International Conference, on Metallurgical Effects of High-Strain-Rate and Fabrication, Plenum Press, New York, 1981.

63. M. R. Staker, “The relation between adiabatic shear instability strain and material properties”, Acta Metallurgica, vol. 29, pp. 681-689, 1981.

64. R. F. Recht and T.W. Ipson, “Ballistic Perforation Dynamics”, Journal of Applied Mechanics, vol. 30, pp. 384-390, 1963.

65. A. Zurek, “The study of adiabatic shear band instability in a pearlitic 4340 steel using a dynamic punch test”, Metallurgical and Materials Transactions A, vol. 25, pp. 2483-2489, 1994.

66. Y. B. Xu, W. L Zhong, Y.J. Chenb, L.T. Shen, Q. Liu, Y.L. Bai and M.A. Meyers, “Shear localization and recrystallization in dynamic deformation of 8090 Al–Li alloy”, Materials Science and Engineering A, vol. 299, pp. 287-295, 2001.

67. Q. Li, Y.B. Xu and M.N. Bassim, “Dynamic mechanical behavior of pure titanium”, Materials Processing Technology, vol. 155-156, pp. 1889-1892, 2004.

68. B. Y. Solomon, A. Khan, N. Bassim, “Microscopical study of the formation of adiabatic shear bands in 4340 steel during dynamic loading”, Philosophical Magazine, vol. 93, 2013.

69. G. Owolabi, D. Odoh, A. Peterson, A. G. Odeshi and H. Whitworth, “Measurement of the deformation of aluminum alloys under high strain rates using high speed digital cameras”, World Journal of Mechanics, vol. 3, pp. 112-121, 2013.

70. M. Hatherly and A.S. Malin, “Shear bands in deformed metals”, Scripta Metallurgica, vol. 33, pp. 449-54, 1985.

71. N. Jia, Z.H. Nie, Y. Ren, R.L. Peng, Y.D. Wang and X. Zhao, “Formation of deformation textures in face-centered-cubic materials studied by in-situ high-energy X-ray diffraction and self-consistent model”, Metallurgical and Material Transactions A, vol. 41, pp. 1246-54, 2010.

72. T. Kamijo and A. Fujiwara, “Shear bands in high purity aluminum”,Scripta Metallurgica Materials, vol. 25, pp. 949-954,1991.

73. R.J. Asaro and A. Needleman, “Flow localisation in strain hardening in crystalline solids”, Scripta Metallurgica, vol. 18, pp. 429-435, 1984.

74. P. Leech, “Observations of adiabatic shear band formation in 7039 aluminum alloy”, Metallurgical Transactions A, vol. 16, pp. 1900-1903, 1985.

75. K. Morii, H. Mecking and Y. Nakayama, “Development of shear bands in FCC single crystals”, Acta Metallurgica, vol. 33, pp. 379-86, 1985.

76. S.J. Pérez-Bergquist, E.K. Cerreta, C.P. Trujillo and A. Pérez-Bergquist, “The dynamic and quasi-static mechanical response of three aluminum armor alloys: 5059, 5083 and 7039”, Materials Science and Engineering A, vol. 528, pp. 8733-8741, 2011.

77. N. Jia, P. Eisenlohr, F. Roters, D. Raabe and X. Zhao, “Orientation dependence of shear banding in face-centered-cubic single crystals”, Acta Matererials, vol. 60, pp. 3415-34, 2012.

78. Y.G. Kim, B. Hwang, S. Lee, W.G. Kim andD.H. Shin, “Dynamic deformation and fracture behavior of ultrafine-grained aluminum alloy fabricates by equal-channel angular pressing”, Metallurgical and Materials Transactions A, vol. 36, pp. 2947-2955, 2005.

79. A.G. Odeshi, M.N. Bassim and M. Bolduc, “Dynamic impact behavior of 6061-T6 and 5083-H131 aluminum alloys”, 12th International Conference on Fracture, Ottawa, 2009.

80. A.G. Odeshi, A.O. Adesola and A.Y. Badmos, “Failure of AA6061 and 2099 aluminum alloys under dynamic shock loading”, Engineering Failure Analysis, vol. 35, pp. 302-314, 2013.

81. ASTM standard E209, “Standard Practice for Compression Tests of Metallic Materials at Elevated Temperatures with Conventional or Rapid Heating Rates and Strain Rates”, ASTM International, West Conshohocken, PA, 2010, DOI: 10.1520/E0209-00R10, www.astm.org.

82. ASTM Standard E9, “Standard Test Methods of Compression Testing of Metallic Materials at Room Temperature”, 2009, ASTM Internathinal, West Conshohocken, PA, 2009, DOI: 10.1520/E0009-09, www.astm.org.

83. T. Sheppard and A. Jackson, “Constitutive equations for use in prediction of flow stress during extrusion of aluminum alloys”, Materials Science and Technology, vol. 13, pp. 203-209, 1997.

84. X.J. Wu and D.A. Gorham, “Stress equilibrium in the split Hopkinson pressure bar test”, 5th International Conference on Mechanical and Physical Behavior of Materials under Dynamic Loading, Franc, 1997.

85. G.F.V. Voort, “Metallography: principles and practice”, ASM International, Materilas Park Ohio, pp. 752, 1984.

86. X. Huang, H. Zhang, Y. Han, W. Wu and J. Chen, “Hot deformation behavior of 2026 aluminum alloy during compression at elevated temperature”, Materials Science and Engineering A, vol. 527, pp. 485-490, 2010.

87. H.R. Rezaei Ashtiani, M.H. Parsa and H. Bisadi, “Effects of initial grain size on hot deformation behavior of commercial pure aluminum”, Materials and Design, vol. 42, pp. 478-485, 2012.

88. H. J. McQueen, T.G. Langdon, H.D. Merchant, J.G. Morris, and M.A. Zaidi, “Hot deformation of aluminum alloys”, TMS-AIME, Warrendale, PA, pp. 31-54, 1991.

89. M.M. Farag, C.M. Sellars and W.J. McG, “Tegart, Deformation under hot working conditions” Iron and Steel Institute, London, pp. 117–121, 1968.

90. H.R. Rezaei Ashtiani, M.H. Parsa and H. Bisadi, “Effects of initial grain size on hot deformation behavior of commercial pure aluminum”, Materials and Design, vol. 42, pp. 478-485, 2012.

91. N. Haghdadi, A. Zarei-Hanzaki, and H.R. Abedi, “The flow behavior modeling of cast A356 aluminum alloy at elevated temperatures considering the effect of strain”, Materials Science and Engineering: A, vol. 535, pp. 252-257, 2012.

92. S. Srinivasulu and A. Jain, “A comparative analysis of training methods for artificial neural network rainfall–runoff model”, Applied Soft Computing, vol. 6, pp. 295-306, 2006.

93. Z. Zheng and D. Zhu, “Analysis of adiabatic shearing failure mechanism for aluminum matrix composites based on experimental and numerical simulation”, Wuhan University of Technology-Matererial Science, vol. 27, pp. 892-896, 2012.

94. D. Rittel, "A different viewpoint on adiabatic shear localization", Journal of Physics D: Applied Physics 42, vol. 21, pp. 214009, 2009.

95. A.O. Adesola, A.G. Odeshi, and U.D. Lanke, “The effects of aging treatment and strain rates on damage evolution in AA 6061 aluminum alloy in compression” Materials and Design, vol. 45, pp. 212-221, 2013.

96. L.D. Oosterkamp, A. Ivankovic, and G. Venizelos, “High strain rate properties of selected aluminium alloys”, Materials Science and Engineering: A, vol. 278, pp. 225-235, 2000.

97. K. Cho, Y.C. Chi and J. Duffy, “Microscopic observations of adiabatic shear bands in three different steels”, Metallurgical Transaction A, vol. 21, pp. 1161-1175, 1990.

98. T.A.C. Stock and A.L. Wingrove, “The energy required for high-speed shearing of steel”, Journal of Mechanical Engineering Science, vol. 13, pp. 110-115, 1971.

99. G.H. Andrew, H.R. Pak, and M.A. Meyers, “Adiabatic shear localization in titanium and Ti-6 pct Al-4 pct V alloy”, Metallurgical transactions A, vol. 16, pp. 761-775, 1985.

100. M.N. Bassim, “Study of the formation of adiabatic shear bands in steels”, Journal of Materials Processing Technology, vol. 119, pp. 234-236, 2001.

101. B. Hwang, Y.G. Kim, H.S. Lee, S. Lee, B.D. Ahn, D.H. Shin, and C.G. Lee, “Dynamic deformation behavior of ultrafine-grained low-carbon steels fabricated by equal-channel angular pressing”, Metallurgical and Materials Transactions A, vol. 36, pp. 389-397, 2005 .

APPENDIX A

POLYNOMIAL EQUATIONS

This appendix introduces the polynomial equations, which were obtained by fitting the best curves to variation of experimental material constants with true strain for as-cast and homogenized A535 alloy.

$$n = f(\varepsilon) = -16.27 + 682.87\varepsilon - 7452\varepsilon^2 + 35700.53\varepsilon^3 - 78582.12\varepsilon^4 + 64813.34\varepsilon^5$$

$$n' = g(\varepsilon) = 44.3 - 506.53\varepsilon + 3368.65\varepsilon^2 - 10314\varepsilon^3 + 14021.25\varepsilon^4 - 5917.95\varepsilon^5$$

$$\beta(\mathrm{MPa}^{-1}) = h(\varepsilon) = 0.47 - 7.65\varepsilon + 60.75\varepsilon^2 - 241.4\varepsilon^3 + 465.9\varepsilon^4 - 348.3\varepsilon^5$$

$$\alpha(\mathrm{MPa}^{-1}) = j(\varepsilon) = 0.25 - 5.75\varepsilon + 53.77\varepsilon^2 - 232.84\varepsilon^3 + 472\varepsilon^4 - 361.54\varepsilon^5$$

$$\ln A = k(\varepsilon) = -66.03 + 2775.33\varepsilon - 30979.43\varepsilon^2 + 157491.2\varepsilon^3 - 368109.61\varepsilon^4 + 320900.2\varepsilon^5$$

$$Q(kJ/mol) = l(\varepsilon) = -82.04 + 9717.62\varepsilon - 122114.8\varepsilon^2 + 673874.8\varepsilon^3 - 1668869.55\varepsilon^4 + 1519226.84\varepsilon^5$$

APPENDIX B

COEFFICIENTS OF THE POLYNOMIAL EQUATIONS

This table summarizes the coefficients of the polynomial functions for n, n', β (MPa^{-1}), α (MPa^{-1}), ln$A$ and Q(kJ/mol) for as-cast and homogenized A535 alloy.

Table B. Summary of polynomial functions coefficients for n, n', β, α, ln$A$ and Q for as-cast and homogenized A535 alloy.

n	n'	β	α	ln$A$	Q
f_0	g_0	h_0	j_0	k_0	l_0
-16.27	44.3	0.47	0.25	-66.03	-82.04
f_1	g_1	h_1	j_1	k_1	l_1
682.87	-506.53	-7.65	-5.75	2775.33	9717.62
f_2	g_2	h_2	j_2	k_2	l_2
-7452	3368.65	60.75	53.77	-30979.43	122114.8
f_3	g_3	h_3	j_3	k_3	l_3
35700.53	-10314	-241.4	-232.84	157491.2	673874.8
f_4	g_4	h_4	j_4	k_4	l_4
-78582.12	14021.25	465.9	472	-368109.61	-1668869.55
f_5	g_5	h_5	j_5	k_5	l_5
64813.34	-5917.95	-348.3	-361.54	+320900.2	+1519226.84

APPENDIX C

COMPARISON OF THE CALCULATED AND THE MEASURED TRUE STRESS VALUES

This appendix contains of tables, which compare the calculated (σ_C) and the measured (σ_C) true stress values with corresponding relative error percentage at different strain rates, temperatures and strains for as-cast and homogenized A535 aluminum alloy.

Table C.1. Comparison of the calculated ($\sigma_{C)}$ and measured (σ_M) true stress values for as-cast and homogenized A535 at strain rate of 0.005 s^{-1}.

ε	*T* (K)	σ_C	σ_M	Relative error (%)
0.05	473	128.75	129.75	0.77
	573	124.66	115.7	-7.2
	623	81.36	80.93	-0.53
	673	25.4	69.5	173.5
0.1	473	190.52	187.3	-1.68
	573	152	137.92	-9.26
	623	87.45	88.47	1.16
	673	33	67.2	103.57
0.15	473	238.81	240.64	0.76
	573	171.5	151.4	-11.72
	623	99.1	105.7	6.63
	673	35.11	75.93	116.27
0.2	473	291.3	305.05	4.72
	573	192.34	180.16	-6.33
	623	111.77	125.6	12.37
	673	45.6	92.96	103.87
0.25	473	349.8	355.84	1.72
	573	221.43	205.81	-7.05
	623	130.31	139.6	7.12
	673	54.62	100.94	52.94
0.3	473	419.84	419.7	-0.04
	573	257	237.56	-7.56
	623	153.8	168.54	9.58
	673	66	110.5	102.32
0.35	473	508.04	527.3	3.78
	573	303.02	301.12	-0.62
	623	184.7	201.8	9.25
	673	84.74	142.3	67.87
0.4	473	627.84	613.6	-2.26
	573	372.91	359.8	-3.51
	623	233.52	263.5	12.82
	673	112.15	181.44	61.78

Table C.2. Comparison of the calculated ($\sigma_{C)}$ and measured (σ_M) true stress values for as-cast and homogenized A535 at strain rate of 0.05 s^{-1}.

ε	*T* (K)	σ_C	σ_M	Relative error (%)
0.05	473	131	140.37	7.15
	573	130.52	115.7	-11.35
	623	110.08	98.45	-10.56
	673	68.8	74.92	8.9
0.1	473	200	207.1	3.55
	573	168.3	146.76	-12.8
	623	130.9	117.83	-9.98
	673	79.72	85	6.60
0.15		245	270.2	10.29
	473	199.41	171.75	-13.86
	573	150.84	134.6	-10.76
	623	89.77	98.63	9.86
	673			
0.2		320	340.3	6.34
	473	233.21	215.4	-7.63
	573	172.8	168	-2.77
	623	105.24	116.8	10.96
	673			
0.25		385	393.07	2.09
	473	272.51	243.04	-10.81
	573	197.86	186.01	-5.94
	623	121.52	137.7	13.32
	673			
0.3		470	464.36	-1.19
	473	318.8	282.25	-11.46
	573	229.3	213.14	-7.04
	623	143.7	154.45	7.47
	673			
0.35		540	589.63	9.19
	473	372.88	363.45	-2.52
	573	272	277.6	2.05
	623	179.5	194.52	8.36
	673			
0.4		670	671.23	0.18
	473	457.33	417.43	-8.72
	573	332.88	321.01	-3.53
	623	227.1	239.07	5.27
	673			

Table C.3. Comparison of the calculated ($\sigma_{C)}$ and measured (σ_M) true stress values for as-cast and homogenized A535 at strain rate of 0.5 s^{-1}.

ε	*T* (K)	σ_C	σ_M	Relative error (%)
0.05	473	150.6	151	0.26
	573	132	115.6	-12.41
	623	112	102.17	-8.77
	673	96.7	90.73	-6.16
0.1	473	225.84	226.91	0.47
	573	173.9	154.19	-11.33
	623	150	134.2	-10.54
	673	102	103.8	1.75
0.15	473	286.52	299.8	4.63
	573	203	201.3	-0.84
	623	175	163.95	-6.30
	673	139.6	132.35	-5.18
0.2	473	345	375.56	8.85
	573	240	250.64	4.43
	623	210	203.23	-3.22
	673	162.6	162.88	0.17
0.25	473	413.6	430.30	4.03
	573	290	280.3	-3.35
	623	240	223.32	-6.95
	673	191.23	174.85	-8.56
0.3	473	494.5	509.05	2.94
	573	340	326.95	-3.83
	623	279	257.82	-7.59
	673	221.13	199	-10.01
0.35	473			
	573	588.82	651.97	10.72
	623	390	425.78	9.17
	673	342	339.94	-0.60
		266.61	266.84	0.086
0.4	473	711.84	728.9	2.34
	573	497.62	475.07	-4.53
	623	422.3	378.73	-10.31
	673	327.5	296.71	-9.4

Table C.4. Comparison of the calculated ($\sigma_{C)}$ and measured (σ_M) true stress values for as-cast and homogenized A535 at strain rate of 5 s^{-1}.

ε	*T* (K)	σ_C	σ_M	Relative error (%)
0.005	473	161.4	161.61	0.13
	573	140	126.23	-9.83
	623	130.9	112.8	-13.82
	673	108	101.35	-6.14
0.1	473	237.54	246.72	3.86
	573	191.9	173.93	-9.36
	623	162	146.4	-9.63
	673	133	123.11	-7.43
0.15	473	296.4	329.36	11.12
	573	230.65	230.84	0.082
	623	188.12	193.46	2.84
	673	150	161.7	7.8
0.2	473	365.53	410.8	12.38
	573	270.53	288.7	6.71
	623	216.63	243.63	12.46
	673	176	196.17	11.46
0.25	473	433.3	467.53	7.9
	573	320.53	317.50	-0.94
	623	250.44	260.54	4.03
	673	195	212.05	8.74
0.3	473	512.4	553.75	8.06
	573	375.6	371.64	-1.05
	623	289	302.5	4.67
	673	230	243.65	5.93
0.35	473	611.6	682.4	11.57
	573	449.5	488.13	8.6
	623	346.45	380.63	9.86
	673	275	304.62	10.77
0.4	473	733.2	786.52	7.27
	573	545.83	532.71	-2.4
	623	423.75	436.37	2.97
	673	330	354.34	7.37